



Managing Inverted Arch Heaving in Sanlian Tunnel: Analysis of Inverted Arch Structure Utilizing Prestressed Anchor Rods

Yiming Wang · Thevaneyan Krishta David ·
Hazrina Mansor · Jianan Guan

Received: 12 January 2024 / Accepted: 27 March 2024 / Published online: 9 April 2024
© The Author(s), under exclusive licence to Springer Nature Switzerland AG 2024

Abstract The inverted arch heaving is detrimental to the structural safety of tunnels and can cause operational accidents. It is necessary to perform the research on maintenance strategies of inverted arch heaving to ensure the structural safety of tunnels. This paper took the Sanlian Tunnel in Southwest China as the engineering background, and the goals of this research were to explore the cause and maintenance of the inverted arch heaving in tuff stratum. The research methodology in this paper includes numerical simulation and field observations. Proposing maintenance measures for inverted arch heaving in tuff formation and grasping the long-term stress characteristics of the inverted arch structure are the contributions of this study. The inverted arch distress includes heaving (85 mm), cracks, and flexural deformation of reinforcements. FLAC3D numerical simulation shows that the continuous deformation because of the tuff rheological effect has an adverse impact on the inverted arch structure, resulting in cracking and heaving. Deepened inverted arch structure by 65 cm combined with 8 m-long prestressed anchor

rods were adopted to control the distress. The effectiveness of the maintenance approach was assessed through field observations lasting for three years. Influenced by the long-term rheology of the tuff, the stresses in the inverted arch increased rapidly at first, then slowly, and gradually stabilized two years after the construction was completed. The maximum stress of prestressed anchor rods, steel arch frames, initial support concrete, and secondary lining concrete were 84.53 MPa, 22.40 MPa, 13.35 MPa, 7.20 MPa, respectively, which were less than the allowable stress (namely 210 MPa, 160 MPa, 23.8 MPa, 32.5 MPa, respectively). Furthermore, the minimum safety factor (namely 6.75) of the reinforced inverted arch met the requirements (>2.4) specified by the Code for Design of Railway Tunnel. The reported findings validate the overall safety of the inverted arch structure following the implementation of control measures, demonstrating the efficacy of these measures in effectively addressing the identified issues. The proposed maintenance strategies and revealed long-term stress characteristics of inverted arch structure in this work can be referenced for construction of tunnels in tuff formation.

Y. Wang · T. Krishta David (✉) · H. Mansor
School of Civil Engineering, College of Engineering,
Universiti Teknologi MARA (UiTM), Shah Alam,
Malaysia
e-mail: thevaneyan@uitm.edu.my

Y. Wang · J. Guan
College of Civil Engineering, Henan University
of Engineering, Zhengzhou, China

Keywords Inverted arch · Crack and heaving ·
Numerical simulation · Control measures · Field
monitoring

1 Introduction

Tunnels have been increasingly used in railway engineering globally and especially in China (Trabucchi et al. 2020; Kuang et al. 2022). By the end of 2021, there were 17,532 railway tunnels spanning 21,055 km in operation (Gong et al. 2022). With the rising number of tunnels, lining defects are increasingly being reported. Tunnel defects, including cavities, cracks, and peeling, have contributed to severe accidents (Kuang et al. 2022; Chen et al. 2023; Elbady et al. 2024). For instance, Lin et al. (2020) reported that water leakage from lining cracks affected the safety of train operation in the Kaiyuan Tunnel in China. Thus, it is necessary to pay attention to the problem of tunnel defects and ensure tunnel maintenance is proportionate to its operational lifetime.

In recent years, numerous reports involving inverted arch uplift and cracks have been recorded (Ma et al. 2020; Han et al. 2021; Zhang et al. 2024). Yang et al. (2019) reported that the floor of the Liu-hai roadway had an uplift during operation, with maximum uplift of 326 mm, resulting in damage to the bottom structure. Xu et al. (2021) reported that the crack and uplift of the inverted arch filling layer resulted in the train shaking during operation. Thus, it is crucial to establish effective countermeasures for addressing the inverted arch heaving distress. This involves exploring mechanism of inverted arch heaving, proposing maintenance measures that mitigate the inverted arch distress, and examining the effectiveness of the proposed maintenance technologies. Most existing studies focus on tunnel arch-lining distress, with little research on the causes and maintenance of inverted arch lining distress (Lin et al. 2020; Ouyang et al. 2023; Abdellah 2024). Therefore, it is necessary to perform the research on the cause, maintenance, and maintenance effect of the inverted arch heaving distress.

In most cases, the causes of tunnel diseases are studied through field investigation or laboratory model tests (Gilbert and Bernard 2018; Agarwal and Sarkar 2024; Petraroia et al. 2024). Song et al. (2019) studied the development characteristics of cracks in tunnel lining in the loose ground through field investigations and laboratory model tests. The development character of cracks was obtained in this study. Du et al. (2020) conducted an in-situ stress test to reveal

the cause of the tunnel floor heave in mudstone. The research result shows that the floor heave of the invert can be divided into three phases namely: slight heaving, moderate heaving and severe heaving. Min et al. (2021) studied the adverse influence of cracks on the inverted arch using experimental tests, and revealed that cracks weakened the bearing capacity of the concrete lining. Kong et al. (2024) proposed the prefabricated inverted arch structure, and conducted experimental tests for four joint types, and revealed that Z-joint was best suited for the novel tunnel structure. However, actual field or laboratory test research on the mechanism of inverted arch disease can be costly and time-consuming (Zertsalov et al. 2022; Ding et al. 2023). Alternatively, numerical simulation can be used as means to examine the aetiology of tunnel lining disease. Festi et al. (2023) studied the characteristics of lining defects in tunnels through numerical simulation. They revealed that the tunnel spandrel had a higher maximum tension stress compared to other parts of the tunnel structure, and thus a large number of cracks appeared in the tunnel spandrel. Jia et al. (2023) studied the mechanism and maintenance of tunnel lining distress caused by seepage through numerical investigation. They revealed that groundwater seepage softened the surrounding rocks and adversely affected the lining structure, and that grouting should be improved to minimize the occurrence of lining defects. However, these two studies had not revealed the characteristics and mechanism of inverted arch distress. Thus, the causes of inverted arch heaving distress will be explored through numerical analysis in this paper.

There is limited research on the maintenance of inverted arch distress (Han et al. 2021; Małkowski et al. 2022; Li et al. 2022). Ma et al. (2020) investigated the cause of inverted floor heave in Gaopo Tunnel in a slightly inclined stratum with mudstone and suggested the double-layered primary support structure to control the inverted arch distress. The control strategies were found to be effective according to the field monitoring data. Han et al. (2021) proposed the "Anchor-Grouting-Drainage" treatment measure to reinforce the tunnel bottom structure. However, no field monitoring data was found in this study to demonstrate the effectiveness of this treatment. Chang et al. (2024a, b) proposed the "miniature steel pipe piles+H-shaped steel support" to control the inverted arch heaving, and conducted the deformation

monitoring of the tunnel pavement to assess the maintenance effect. Nevertheless, they did not perform the field observation of stresses in the reinforced inverted arch to grasp the stress characteristics.

Tuff is a kind of soft rock, fissures are widely distributed, the material has low strength, and there is significant plastic deformation in tuff formation. Due to the tuff's rheological properties, the amount of deformation is significant and lasts for a long time after the tuff is excavated (He et al. 2024). The support structure may undergo large deformations and cracking, when tunneling in soft tuff surrounding rocks (Reddy et al. 2020; Yousif and Karakouzian 2023). Zhang et al. (2024) proposed grouting and applying the inverted arch pipe pile to control the inverted arch heaving in soft mudstone stratum. However, whether this construction scheme is applicable to tuff strata is not mentioned in their study. Regarding tunnels excavated in weathered tuff stratum, He et al. (2024) proposed the optimized construction method, namely "middle first and side later" double side heading method, yet, control measures for inverted arch heaving was not proposed in their study. Chang et al. (2024a, b) proposed to strengthen the arch foot support and improve drainage to control the inverted arch uplift of the tunnel in loess stratum. Nevertheless, their study did not address the countermeasures for inverted arch disease in tuff formation. The tuff formation is a geological condition often encountered in tunnel engineering in China (Fei et al. 2023). Performing the research on the control technology of inverted arch heaving in tunnels excavated in tuff formation is of great value for engineering application.

Few existing studies use numerical modelling or short-term on-site assessments to validate the efficiency of disease control methods (Li et al. 2020; Haque and Ansary 2023; Yue et al. 2023). By using displacement monitoring for up to 15 days, Cao et al. (2018) validated the effectiveness of a strengthened support structure to control the large deformation and failure of the tunnel's primary support. Based on this study, the countermeasure could guarantee the structural safety under construction. Using the numerical simulation, Liu et al. (2020) evaluated the effectiveness of maintenance for cracking and spalling concrete, yet, it has not been proven by the field-measured data. Ye et al. (2020) conducted the safety check calculation for the Liupanshan tunnel

after reinforcement and evaluated the effectiveness of maintenance through the numerical simulation, whereas no field-measured data validated the efficiency. Zhang et al. (2020) analyzed the effectiveness of grouting to reinforce lining defects by fitting a response surface function; nevertheless, the effect of the control measures on the long-term structural safety remains unclear. Based on their study, long-term on-site monitoring can better reflect the stress state of the concrete lining structure. However, a limited study is being conducted on the long-term monitored data, which is a concern (Li et al. 2021; Ghadernjad and Moosavi 2022; Rao et al. 2023). As a result, substantial research on the inverted arch illness in tuff formation through long-term measured data is required to examine maintenance effects, which is the focus of this paper.

Based on the previous research results, some aspects related to the cause and maintenance of lining distress need to be improved. Firstly, previous studies have tended to investigate the tunnel arch diseases, such as insufficient lining thickness and cavities underneath the lining. There are fewer studies on the inverted arch distress, yet. Then, in the extant literature, there are few studies on the causes and maintenance strategies of the inverted arch heaving in tuff formations. Finally, previous studies often implement numerical simulations or short-term on-site observations to analyze the effectiveness of the proposed maintenance measures. However, few studies used long-term monitoring to examine the stress characteristics of tunnel structures, and evaluate the effectiveness of the proposed maintenance.

Considering the antecedent research endeavours, this paper uses field investigation data collected from the Sanlian (SL) Tunnel in Southwest China to investigate the heaving and cracks in the inverted arch on the tuff formation. Then, numerical simulation analyses were used to study the cause of the inverted arch disease on the tuff formation. Next, the control measures were proposed based on the numerical simulation results. Later, the maintenance of the inverted arch was conducted, and strain gauges were arranged on the inverted arch during the maintenance process. Then stresses of the inverted arch structure was observed continuously for three years, and the field data was collected. Finally, the effectiveness of the maintenance measures is evaluated according to the field observation results.

Compared with the existing research results, this study is an improvement in the following three aspects. Firstly, factors that influence the inverted arch disease are examined through numerical simulation, and the material properties are obtained from the experimental test. Secondly, the maintenance of inverted arch heaving is proposed for the tunnel excavated in tuff deformation, which is widely distributed in Southwest China. Thirdly, the stress of prestressed anchor rods, the contact stress between surrounding rocks and the initial support, the stress of the steel arch frame, the stress of the initial support concrete, and the stress of the secondary lining concrete are observed for three years after maintenance. This comprehensive and long-term on-site monitoring provides a true picture of the stress state of the inverted arch structure after maintenance. The effectiveness of the proposed maintenance can be evaluated based on the field monitoring results.

Cases of inverted arch heaving in tuff formation have been repeatedly reported, and significantly impact structural safety of tunnels. Therefore, it is necessary to carry out the research on the countermeasures of inverted arch heaving in tuff formation. Existing studies lack field monitoring of long-term stress characteristics of the inverted arch structure in tuff formation, which is the research gap. In this study, long-term field observations were conducted for three years to capture stress characteristics of the inverted arch structure and to evaluate the

effectiveness of the proposed maintenance measures. This study is expected to provide a reference for the design and construction of tunnels in tuff formation.

2 Tunnel Background

2.1 Tunnel Overview

SL tunnel was chosen as the case study in this work. The tunnel was designed as a single tunnel with a double track to accommodate the design speed of 160 km per hour. SL Tunnel is an extra-long railway tunnel of 12214 m (DK300+387~DK312+601). "DK" is the abbreviation of "Distance Kilometre", indicating the distance (km) from the starting point of the railway. The entrance and exit mileage are 300.387 km and 312.601 km from the starting point of the railway, respectively. The entrance elevation is about 1850 m, and the exit elevation is about 1960 m. With a total length of 495 m, the tunnel between DK305+945 and DK306+440 travels through the tuff formation between the Mujia Fault and Shangtumu Fault.

The tunnel profile and the concrete lining are shown in Figs. 1 and 2, respectively. The tunnel is designed with an inverted arch, and the concrete lining structure consists of the primary and secondary lining. For the initial support of the arch wall and inverted arch, C25 shotcrete with a thickness of

Fig.1 Sanlian tunnel profile

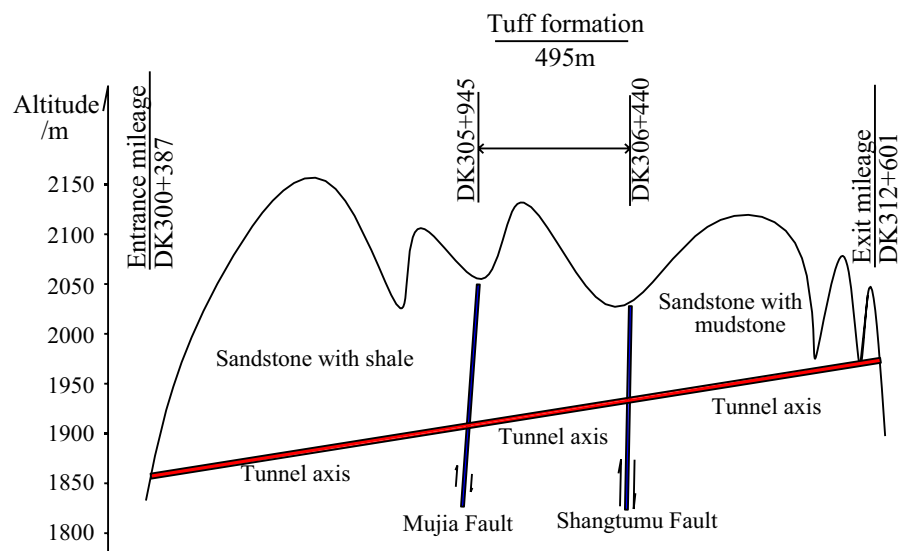
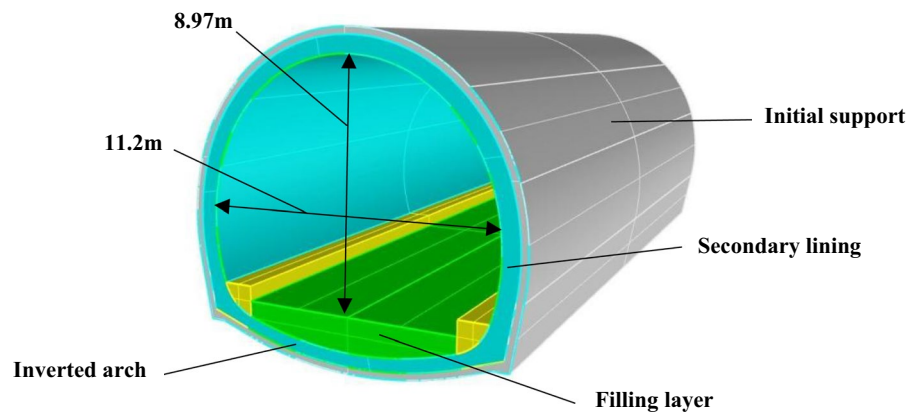


Fig. 2 Lining structure of Sanlian tunnel



25 cm was employed. Steel meshes with a spacing of 0.6 m×0.6 m and an anchor rod system with 4 m length were adopted as the initial support. The secondary lining of the arch wall and the inverted arch was constructed out of C35 reinforced concrete with a thickness of 55 cm and 25 mm diameter primary reinforcement. The inverted arch was backfilled with C30 concrete. The inner contour of the tunnel lining on the tuff formation is 8.97 m high and 11.2 m wide.

2.2 Problem of the Inverted Arch Heaving

The construction work of the SL tunnel began in April 2011. As this was an extra-long tunnel, it took four years to complete the tunnel construction. The SL tunnel was completed in April 2015, and the tunnel was monitored after construction. About one year after the inverted arch (DK306+020~DK306+146) was completed, the observation shows that there were different degrees of heaving on the surface layer of the inverted arch filling, shown in Fig. 3a. The maximum heaving was 85 mm at DK306+040, shown in Fig. 3b. The section DK306+020 to DK306+080 had a higher invert heaving than the other section.

About one year after the SL tunnel was completed, the geological condition within the tuff deposit (DK306+020~DK306+146) was fragmented, with cracks forming and a considerable risk of instability. The cracks were first observed in May 2016. The prescribed tunnel segment had three long cracks: Crack A, B and C. The crack width was measured to be about 10 mm. The widest part of the crack was about 100 mm, located at Dk306+040. Figure 4 illustrates the location of the prescribed cracks.

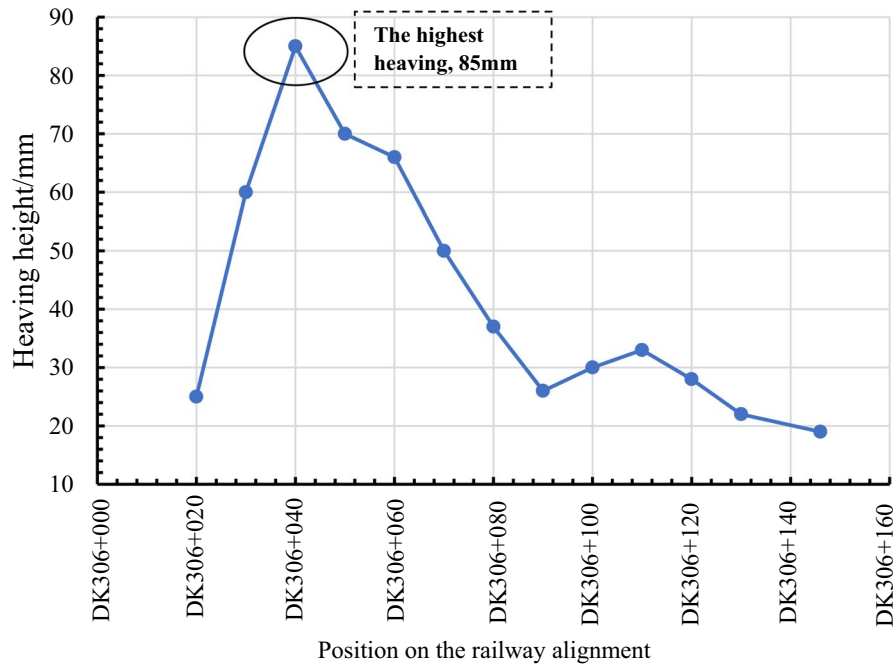
The broken tuff section at Dk306+040~Dk306+045 was subjected to additional inspection. The filling layer and inverted arch were smashed to break, and the condition beneath the broken smashed and inverted arch layer was assessed. As illustrated in Table 1, longitudinal cracks formed, and the primary reinforcement was bent.

3 Numerical Analysis of the Inverted Arch Heaving and Crack

3.1 Numerical Model and Material Properties

3.1.1 Working Conditions and Numerical Model

A fast Lagrangian analysis of Continua in 3 dimensions (FLAC3D) numerical modelling software was used to investigate the cause of inverted arch heaving and cracking. In this work, a selected cross-section of the tunnel (i.e. at DK306+080) was modelled in a two-dimensional (2D) space using a hexahedral element. The inverted arch heaving occurred in tuff formation in the Sanlian tunnel. Tuff is a kind of soft rock, and is characterized by the rheology and large plastic deformation (Nicotera and Russo 2021). Rheology refers to the phenomenon of increasing deformations of rocks with time under constant stresses (He et al. 2024). In order to investigate whether the rheology caused the inverted arch heaving, two working conditions were proposed in this study. In condition 1, rheology is not considered in tuff formation. In contrast, rheology is considered in tuff formation in condition 2.



(a) Heaving height of the inverted arch at DK306+020 ~ DK306+146



(b) Image for the highest heave height at DK306+040

Fig. 3 Inverted arch heaving in the Sanlian tunnel. **a** Heaving height of the inverted arch at DK306+020~DK306+146. **b** Image for the highest heave height at DK306+040

The developed cross-section model has a horizontal length of 230 m and a vertical length of 150 m. The buried depth of this section is 200 m. The size and boundary condition of this model is shown in Fig. 5. Boundary conditions were applied to the three perimeter sides of the tunnel, denoted as side AB, side BC, and side CD. Specifically,

side AB and CD were constrained in the translation along the x axis, while side BC was constrained in the z direction. The buried depth of the tunnel was realized by applying the equivalent gravity stress at the top (i.e., side AD) (Qiu et al. 2023; Senthil et al. 2024). The grid of the developed model is shown in Fig. 6.

Fig. 4 Plane expanding image of the cracks on the inverted arch filling

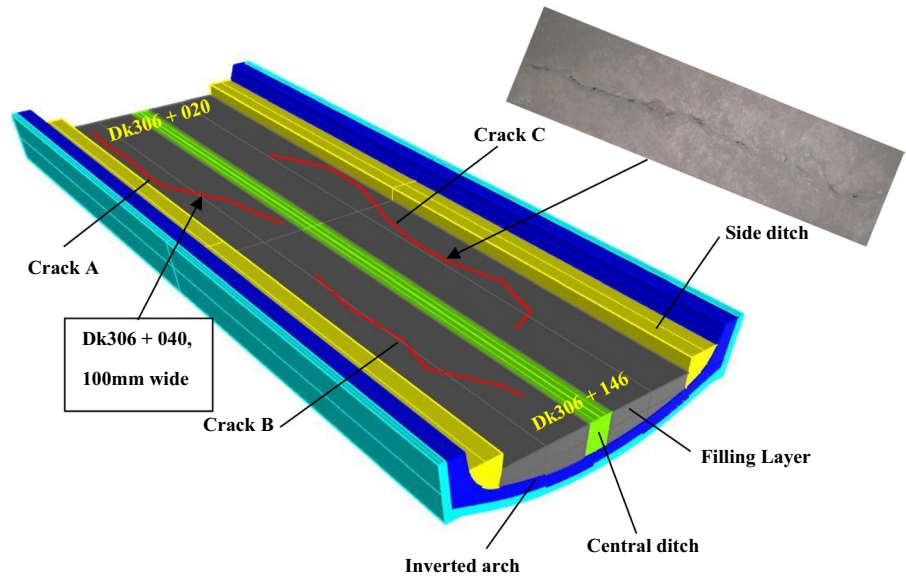


Table 1 Type of inverted arch damage observed in the SL tunnel within one year after completion



Damage	Description	Images
Cracks of an inverted arch	Longitudinal cracks appeared on the top surface of the inverted arch, with a width of 5~15 mm	
Flexural deformation of reinforcement	The 25 mm diameter primary reinforcement exhibited bending in the inverted arch	

Fig. 5 Size and boundary condition of the numerical model

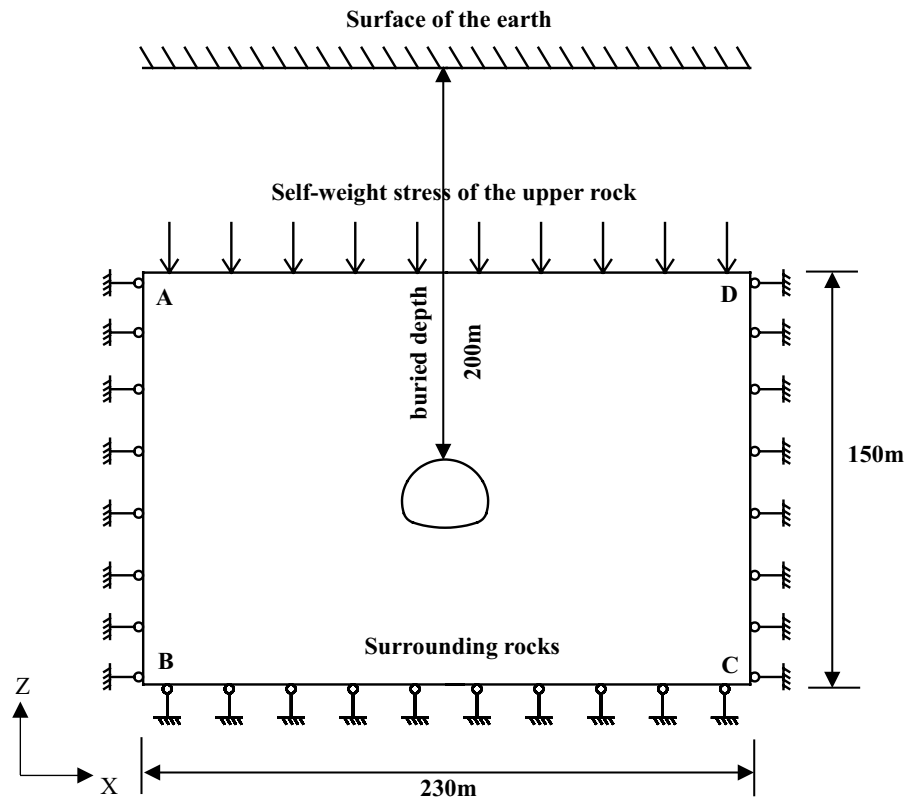
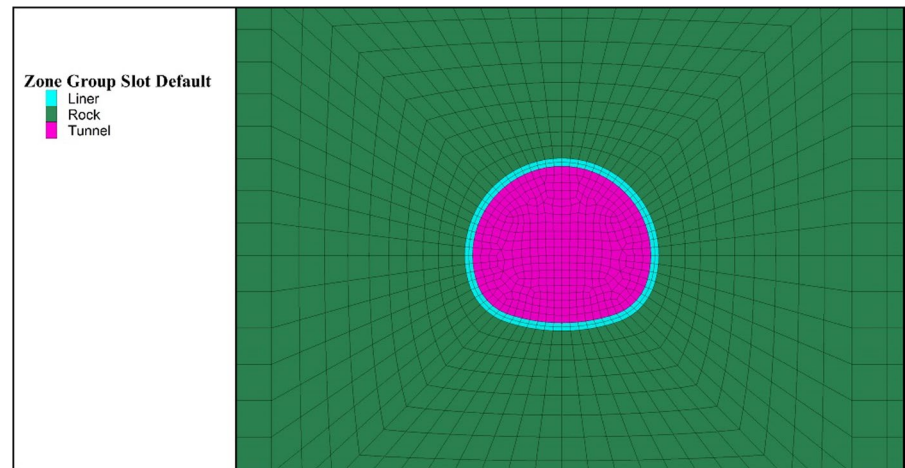


Fig. 6 Grid of the numerical model



3.1.2 Material Properties in Condition 1

In Condition 1, the linear elastic and Mohr-Columb material models are utilized to simulate the tunnel concrete lining and the surrounding rocks. The mechanical properties of the surrounding rocks and the tunnel lining are determined using the Code for

Design of Railway Tunnel (China Railway Eryuan Engineering Group Co.Ltd. 2016). In the geological investigation of tunnels, the surrounding rocks are identified into different classifications. For the design of the tunnel structure, reference can be made to the design scheme of existing tunnels with the same surrounding rock classification. The tuff surrounding

Table 2 Physical properties of surrounding rocks and tunnel lining

Condition	Material	Physical and mechanical parameter
Condition1	Surrounding rocks	$E=1.3\text{ GPa}, \rho=2350\text{ kg/m}^3, \mu=0.35, c=500\text{ kPa}, \varphi=40^\circ$
	lining concrete	$E=30\text{ GPa}, \rho=2500\text{ kg/m}^3, f_c'=16.1\text{ MPa}, f_t=1.52\text{ MPa}, \mu=0.2$

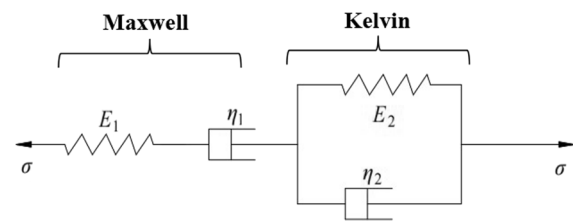


Fig. 7 Schematic diagram of burgers model

rock in this tunnel was classified into Class V, based on the results of the geological investigation. The Code for Design of Railway Tunnel includes the reference values for the mechanical parameters of Class V surrounding rocks. Therefore, the mechanical parameters of tuff formations are taken from these reference values. Table 2 depicts the mechanical properties of the surrounding rocks and the tunnel structure.

3.1.3 Material Properties in Condition 2

According to Chu et al. (2018), Burgers Model could accurately depict the rheological features of soft rock strata. Since tuff is a typical soft rock stratum, the Burgers Model is employed to model the surrounding rocks for working condition 2. The linear elastic model is likewise employed to simulate the tunnel lining, and the mechanical properties of the lining are the same as in Table 2. As shown in Fig. 7, the Burgers Model includes a Kelvin cell series with a Maxwell component. The constitutive equation of the model is shown in Eq. (1) (Chu et al. 2018). In this model (Fig. 7 and Eqs.(1)), e is natural constant, σ is stress, ϵ is strain, t is the rheological time, E_1 is the elastic modulus, E_2 is the viscoelastic modulus, η_1 and η_2 are the viscosity coefficients, respectively.

$$\epsilon = \frac{\sigma}{E_1} + \frac{\sigma}{\eta_1}t + \frac{\sigma}{E_2} \left(1 - e^{-\frac{E_2}{\eta_2}t} \right) \tag{1}$$

The triaxial compression rheological test was carried out in the laboratory to obtain the four parameters, namely E_1 , E_2 , η_1 and η_2 . Four rock samples were taken from the tuff stratum in the SL tunnel. The test followed the Code for Rock Tests in Water and Hydropower Projects (China Renewable Energy Engineering Institute 2020) and consisted of three steps. Step 1: Two samples were used to perform the conventional triaxial compressive strength test, which showed a triaxial compressive strength value of 8.9 MPa. Step 2: Two samples were used to perform the triaxial compression rheological test. A confining pressure of 3.5 MPa was applied, which is consistent with the in-situ stress test result. The axial pressure was applied using a graded incremental loading method. Since the number of loading stages should not be less than 5 (China Renewable Energy Engineering Institute 2020), the difference between 8.9 MPa (shown in Step 1) and 3.5 MPa was divided into 9 equal parts in this test, and the increment of each stage was 0.6 MPa. In the actual test, the axial pressure was applied in accordance with 4.3 MPa, 4.9 MPa, 5.5 MPa, 6.1 MPa, 6.7 MPa, 7.3 MPa, 7.9 MPa, and deformations of samples grew dramatically and ruptured when loaded to 7.9 MPa. Step 3: Since the axial pressure of the rock from the in-situ stress test result was 5.5 MPa, the strain–time curve at 5.5 MPa axial pressure from the triaxial rheological test was analyzed (shown in Fig. 8), and the least square approach (Chu et al. 2018) was used for fitting. The rheological properties of the surrounding rocks obtained from the fitting data were employed, and Fig. 8 depicts the precision of the experimental and fitting results. The rheological properties of surrounding rocks used in Condition 2 are shown in Table 3.

3.1.4 Numerical Analysis Procedure

The simulation procedure consisted of three steps. In Step One, the initial state of the tunnel prior to excavation was modelled and the mechanical parameters (shown in Tables 2 and 3) and boundary conditions (shown in Fig. 5) were assigned to the surrounding rocks. The initial stresses in the surrounding rocks before excavation could be obtained from the calculations in this step. Then, the state of the tunnel after

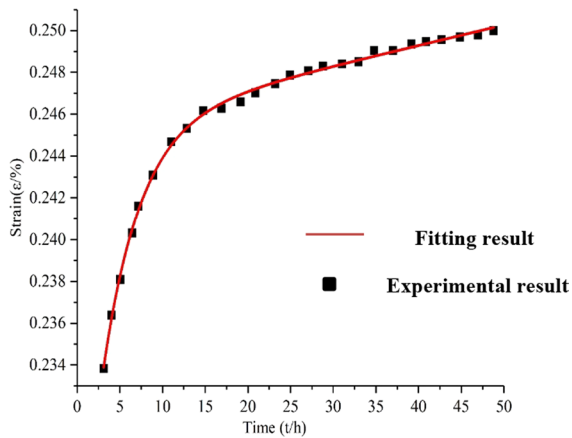


Fig. 8 Experimental and fitting result

Table 3 Rheological properties of surrounding rocks

Material	Maxwell elastic modulus (E_1 \MPa)	Maxwell viscosity coefficient (η_1 \MPa-h)	Kelvin viscoelastic modulus (E_2 \MPa)	Kelvin viscosity coefficient (η_2 \MPa-h)
Surrounding rocks	21.8	43,110.9	177.4	929.9

excavation was simulated in Step Two. 'Null' material model was employed to the elements within the tunnel contour. Next, the state of the tunnel after lining construction was simulated in Step Three. The linear elastic model and material parameters were employed to simulate the lining structure. Stresses and displacements were extracted and analyzed based on the calculation results in this step.

3.2 Analysis of Numerical Result

3.3 Displacement analysis.

The displacement of the adjacent rocks is shown in Fig. 9. The vertical displacement values at four points (refer to a, b, c, d in Fig. 9) are extracted from the numerical simulation and illustrated in Table 4. As shown in Table 4, the displacement values are positive, and these indicate that the surrounding rocks under the inverted arch both move upward in Condition 1 and 2. The heaving at the centerline (refer to point d in Fig. 9b) of the

inverted arch is 42 mm, as shown in Table 4. As can be seen in Fig. 3a, The monitored heaving is 37 mm at DK306 + 080, which is the location of the cross-section numerical model. The numerical simulation result (namely 42 mm) is close to the field monitored displacement (namely 37 mm), indicating that the numerical model is reasonable and the results are reliable. By comparing the displacements at the four points (i.e., a,b,c,d in Table 4), it is found that the heaving displacements in Condition 2 are significantly greater than those in Condition 1. Considering the rheological properties of the tuff formation, the numerical model has caused significant heaving deformation by the surrounding rock and led to the high stress on the inverted arch and forces it to move upward. The deformation of the inverted arch structure can be seen from the cracking effects of the concrete filling layer and heaves. Theoretically, the inverted arch heaving is caused by the long-term rheological deformation of the tuff and the extrusion effect on the inverted arch structure. Therefore, from the analysis, it can be highlighted that the rheology of the tuff may contribute significantly for the heaving of the inverted arch movement.

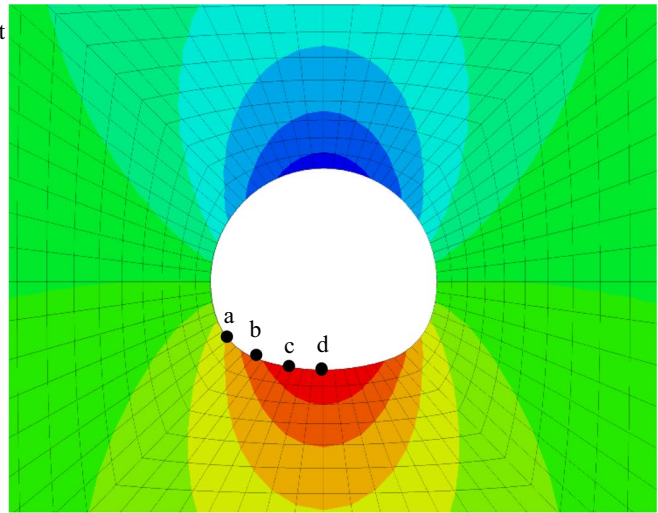
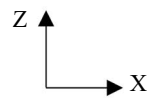
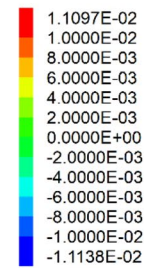
3.4 Stress Analysis

The maximum principal stresses of the inverted arch are shown in Fig. 10. The principal stress values at four zones (refer to A, B, C, D in Fig. 10) are extracted from the numerical simulation and illustrated in Table 5. As shown in Table 5, the principal stress values are negative, and this indicates that the inverted arch is subjected to compressive stresses in Condition 1 and 2. By comparing the principal stress values of the four points (i.e. A,B,C,D in Table 5), it is found that the compressive stresses in Condition 2 are significantly greater than those in Condition 1. It shows that the rheological effects of the surrounding rocks can cause significant increase in the principal stresses of the inverted arch. Then cracks may appear in the inverted arch, and the inverted arch may be damaged.

As a result, it is possible to conclude that the structural design of the SL tunnel crossing the tuff formation has omitted the effect of tuff rheology and its adverse effect on the structure, and the structural design needs to be optimised.

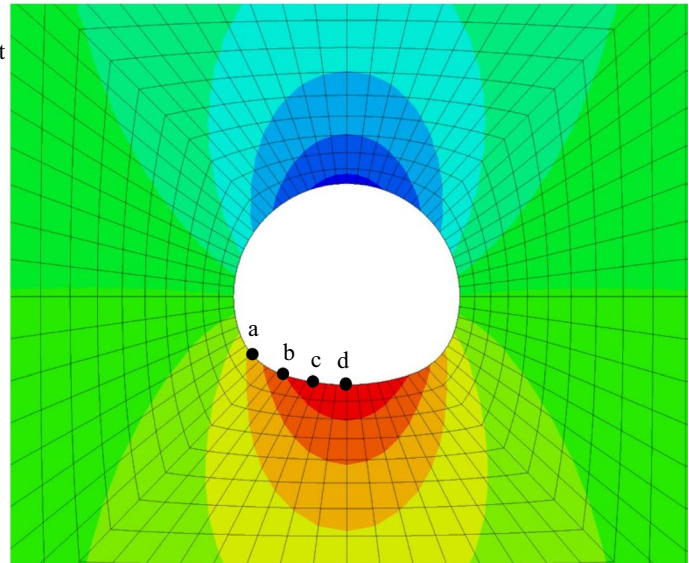
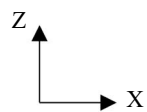
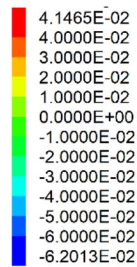
Fig. 9 Displacement results of numerical simulation. **a** Displacement in working condition 1. **b** Displacement in working condition 2

Vertical displacement of surrounding rocks along Z direction (Unit: mm)



(a) Displacement in Working Condition 1

Vertical displacement of surrounding rocks along Z direction (Unit: mm)



(b) Displacement in Working Condition 2

Table 4 Vertical displacement at Point a~d /mm

Serial number	a	b	c	d
Condition 1	8	9.7	10	11
Condition 2	27	36	40	42

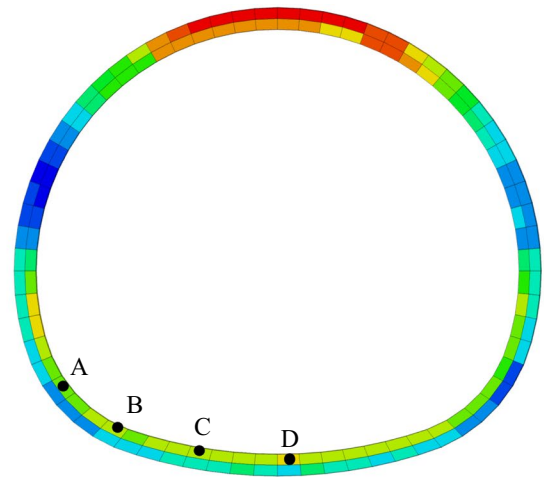
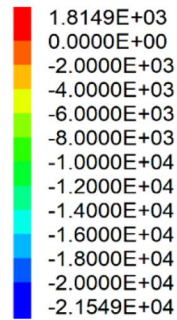
4 Proposed Control Measures of the Inverted Arch

4.1 Design of Control Measures

As the cause analysis shows that the continuous deformation because of the tuff rheological effect has an adverse impact on the inverted arch structure, resulting in cracking and heaving. Thus, rebuilding a deeper inverted arch structure combined with

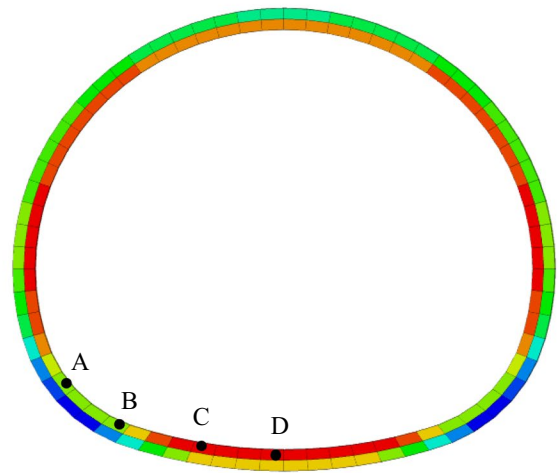
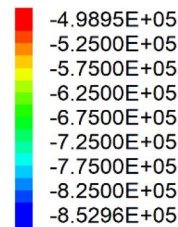
Fig. 10 Lining stress of numerical simulation. **a** Principal stress in working condition 1. **b** Principal stress in working condition 2

Maximum principal stress of lining structure (Unit: Pa)



(a) Principal stress in Working Condition 1

Maximum principal stress of lining structure (Unit: Pa)



(b) Principal stress in Working Condition 2

Table 5 Principal stress at Zoint A~D /kPa

Serial number	A	B	C	D
Condition 1	- 10.54	- 8.47	- 7.04	- 6.64
Condition 2	- 701.62	- 601.77	- 547.59	- 529.66

a prestressed anchor rod is adopted to control the inverted arch distress.

The rebuilt inverted arch after maintenance was deeper than the original one, as shown in Fig. 11. When determining this depth value (i.e., 'h' in

Fig. 11) of the inverted arch after maintenance, three working conditions (namely $h=50$ cm, $h=65$ cm, and $h=75$ cm) were developed through the numerical simulation. The numerical model and material properties were similar to the previous simulation in Sect. 3.1.

The developed working conditions and numerical simulation results are reported in Table 6. Axial forces and bending moments of the inverted arch structure were extracted from the numerical simulation results. Then, safety factors were calculated for five sections (refer to Section A to E, as shown

Fig. 11 Control measures of the inverted arch. **a** Original inverted arch **b** Rebuilt inverted arch

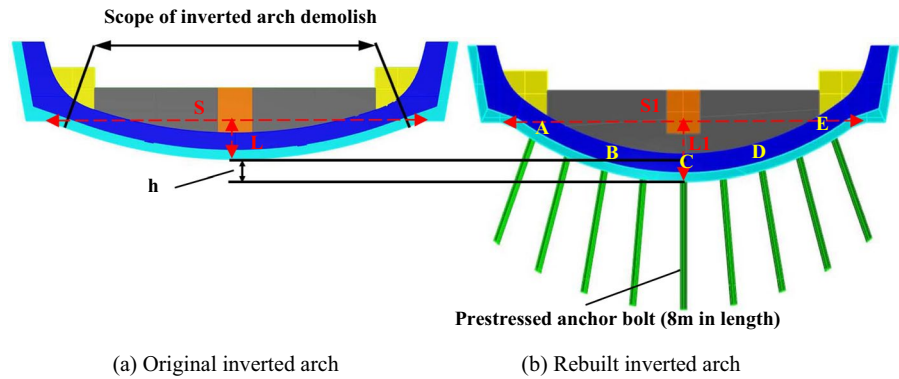


Table 6 Working conditions, inner forces and safety factors of the rebuilt inverted arch

Working condition	Section	A	B	C	D	E
Condition 1 (h=50 cm)	Axial force kN	4899.0	7021.3	8742.1	7021.0	4899.1
	Bending moment \ kN·m	9.7	69.1	20.3	69.2	9.7
	Safety factor	3.95	2.67	2.20	2.67	3.95
Condition 2 (h=65 cm)	Axial force kN	3896.4	6249.8	7975.8	6250.1	3895.2
	Bending moment \ kN·m	8.0	66.4	18.9	66.4	8.1
	Safety factor	4.97	2.98	2.62	2.98	4.97
Condition 3 (h=75 cm)	Axial force kN	3282.6	5221.8	5644.1	5222.0	3282.5
	Bending moment \ kN·m	7.2	49.1	15.3	49.2	7.2
	Safety factor	5.89	3.59	3.50	3.59	5.89

in Fig. 11b) of the inverted arch. The inverted arch is an eccentrically compressed reinforced concrete member that carries axial forces and bending moments in its cross section. Based on the axial forces and bending moments, the safety factors are calculated according to the calculation principle of the section strength check for eccentrically compressed reinforced concrete members with rectangular sections, as illustrated in the Code for Design of Railway Tunnel (China Railway Eryuan Engineering Group Co.Ltd. 2016). The numerical calculation results show that the lining structure is a small eccentric compression member, the safety factor K is calculated according to Eq. (2).

$$KNe = 0.5R_wbh_0^2 + R_gA'_g(h_0 - a') \tag{2}$$

When the axial force N acts between the centers of gravity of steel reinforcement A_g and A'_g , the safety factor is the minimum value obtained from Eqs. (2) and (3), respectively.

$$KNe' = 0.5R_wbh_0^2 + R_gA_g(h'_0 - a) \tag{3}$$

In Eqs. (2) and (3), K is the safety factor; N is the axial force; A_g and A'_g represent the cross-sectional area of the longitudinal tension and longitudinal compression reinforcement, respectively; e and e' represent the distance from the center of gravity of steel reinforcements A_g and A'_g to the point where the axial force is applied, respectively; R_w is the compressive ultimate strength of concrete; R_g is the calculated tensile or compressive strength of steel reinforcements; b and h_0 are the width and effective height of the lining section, respectively; a and a' are the distance from the reinforcement A_g and A'_g to the near side of the section, respectively; h'_0 is the distance between the tensile edge of the section and the center of gravity of the compression reinforcement. The schematic of the safety factor calculation can be seen in the the Code for Design of Railway Tunnel (China Railway Eryuan Engineering Group Co.Ltd. 2016).

From the numerical simulation results, the minimum safety factors of the inverted arch structure in three working conditions are 2.20, 2.62, and 3.50, respectively. The safety factor of the inverted arch must be greater than 2.4 according to the Code for Design on Tunnel of Railway (China Railway Eryuan Engineering Group Co.Ltd. 2016). The surrounding rocks at the bottom of the tunnel need to be excavated prior to the construction of the reinforced concrete inverted arch structure. The deeper the inverted arch, the greater the amount of earth excavated, and the higher the costs related to the construction. The amount of earth excavated and the cost related to the construction is referred to as the quantities of construction. Therefore, the quantities of construction can increase with the increase of the inverted arch depth. Two points should be considered when designing the maintenance scheme: to ensure structural safety and not to increase the quantities too much. Therefore, the final depth value (refer to 'h' in Fig. 11) was determined to be 65 cm.

In this work, the inverted arch along the DK306+020~DK306+146 was rebuilt. The 25-mm diameter and 8 m-long prestressed anchor bolts were applied, and the middle segment of the newly constructed inverted arch was deepened to 65 cm. The rise span ratio was adjusted from 1/12 to 1/6. The rise span ratio (i.e., 1/12) is the ratio between 'L' and 'S' in the original inverted arch shown in Fig. 11a. The

rise span ratio (i.e., 1/6) is the ratio between 'L1' and 'S1' in the rebuilt inverted arch shown in Fig. 11b.

4.2 Construction Process of Control Measures

Prior to removing the original inverted arch, temporary reinforcement was placed appropriately (refer to Fig. 12). Steel foot pipes were installed on both sides of the side walls to prevent the liner structure from slipping downward. While replacing the original inverted arch, transverse temporary supports were installed in the tunnel to prevent excessive introversion of the side wall lining. Table 7 depicts the three processes in the construction of the proposed control measures. First, temporary reinforcing measures were implemented. The inverted arch filling, inverted arch lining, and initial support were then removed in sequence. Later, shotcrete, steel arch, and re-shotcrete were built. The secondary lining of the inverted arch, the inverted arch filling, and the central ditch were built thereafter. The temporary support shall be removed once the secondary lining concrete of the inverted arch has reached the design strength. Six months after the heaving and cracks were observed, the maintenance work for the inverted arch began. During this four-month period, the cause of the inverted arch disease was analyzed, and the control measures were proposed. It took two

Fig. 12 Temporary reinforcement measures

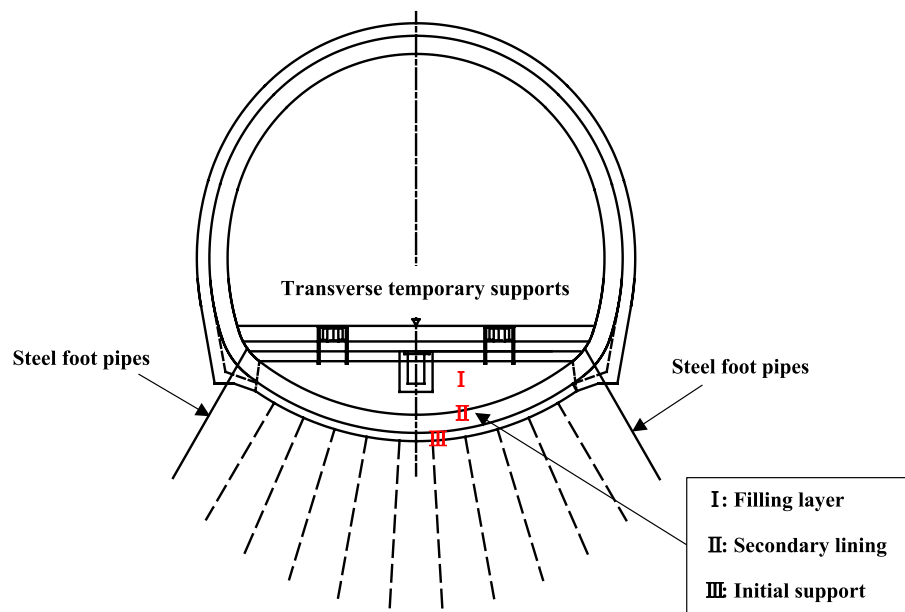

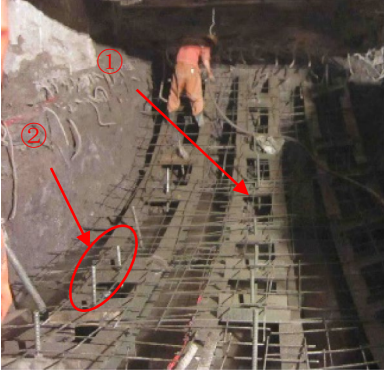



Table 7 The construction process of the proposed control measures

Serial number	Description	Images
Step 1	<ul style="list-style-type: none"> • Construction of transverse temporary supports and steel foot pipes • Remove filling layer, initial support and secondary lining of inverted arch • Excavation to design depth 	
Step 2	<ul style="list-style-type: none"> • Construction of initial support shotcrete, steel arch frame ① and prestressed anchor bolts ② • Construction of secondary lining 	
Step 3	<ul style="list-style-type: none"> • Remove transverse temporary supports • Construction of the Central ditch • Construction of the filling layer 	

months to complete the maintenance work, from November 2016 to December 2016.

5 Maintenance Effect

The effectiveness of the proposed treatment measures was monitored for three years from January 2017 to January 2020 after maintenance. The measuring points and monitoring results are presented in the subsequent sections.

5.1 The Axial Force of the Prestressed Anchor Rod

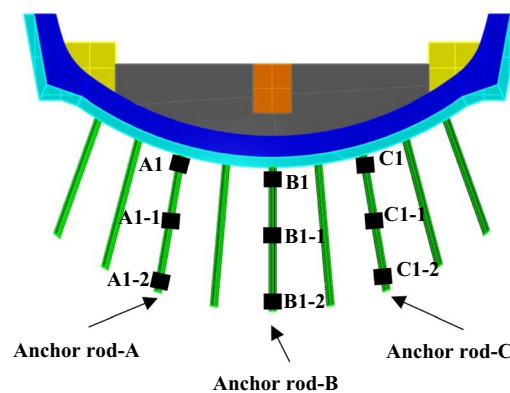
To investigate the axial force of the prestressed anchor rods, the axial force was monitored continuously. As shown in Fig. 13a, anchor rod – A, anchor rod – B, and anchor rod – C were chosen to monitor their axial forces. Three measuring points were arranged for each anchor rod, namely top, middle, and bottom of the anchor rod. Monitoring points A1, A1-1 and A1-2 were arranged in anchor rod-A, points B1, B1-1 and B1-2 were arranged in anchor rod-B, points C1, C1-1 and C1-2 were arranged in anchor rod-C, as illustrated in Fig. 13a. The field installation of the axial force monitoring device can be seen in Fig. 13b.

The analysis results of the axial force at the top of the prestressed anchor rods (refer to Fig. 13) are illustrated in Fig. 14a. The anchor bolt rods, which are in tension, imply that the rheological effect of the tuff does exist, resulting in the upward uplift

of the inverted arch structure. Within the first six months, the axial force of the anchor rod grew rapidly. All the prestressed anchor bolts (i.e. points A1, B1 and C1) at the bottom of the inverted arch produce a downward force on the inverted arch to resist the uplift of the surrounding rock. Later, from the sixth month to the eighteenth month, the axial force of the anchor rods increased slowly. The axial force of the anchor rod (i.e. point A1) increased from 25.589kN to 32.03kN. To ensure the optimum prestressed forces were applied in stabilising the inverted arch, the stress of each part of the structure was then adjusted to achieve balance. Thereafter, during the monitoring period from the eighteenth month to the thirty-sixth month, the increase of the axial forces for all the anchor rods was very small. At the end of the thirty-sixth month, the monitoring results of the prestressed anchor bolts measured at points A1, B1, and C1 were in tension with the axial forces of 32.11kN, 41.471kN and 34.58kN, respectively.

The analysis results of the axial force at the middle of the prestressed anchor rods (refer to Fig. 13) are illustrated in Fig. 14b. The monitored axial force values are all positive, indicating that the prestressed anchor rods are under tension. Within the first six months, the axial force of the anchor rod grew rapidly. The measured axial force in the sixth month at points A1-1, B1-1, and C1-1 was 20.589kN, 32.45kN, and 31.254kN, respectively. Later, from the sixth month to the eighteenth month, the axial force of the anchor rods increased slowly.

Fig. 13 Axial force field testing of the prestressed anchor rod. **a** Measuring points, **b** monitoring device installation

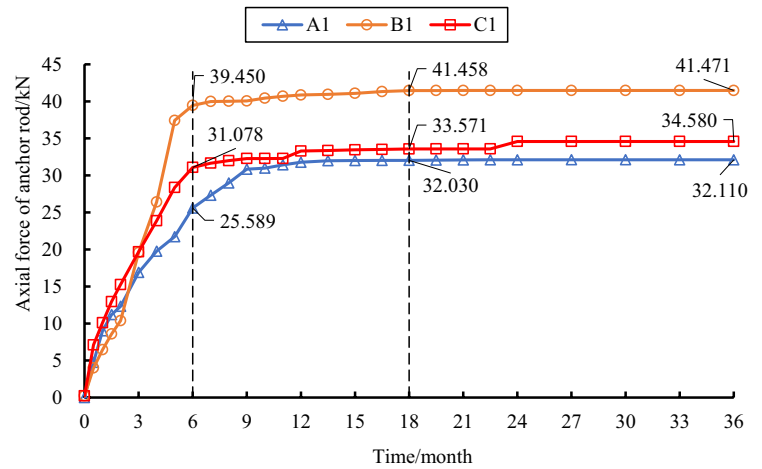


(a) Measuring points

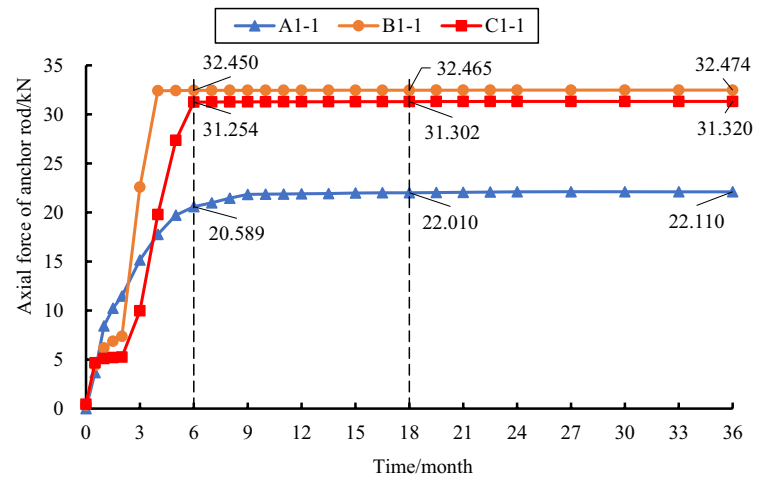


(b) Monitoring device installation

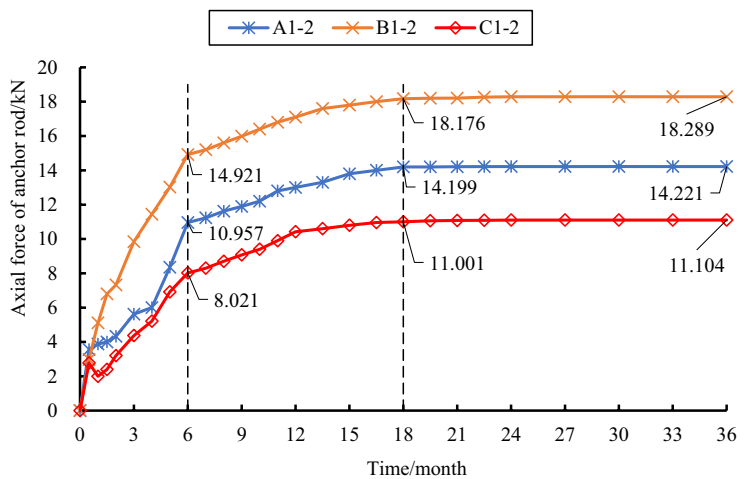
Fig. 14 Axial force of the prestressed anchor rods. **a** Axial force at the top of the prestressed anchor rods, **b** Axial force at the middle of the prestressed anchor rods, **c** Axial force at the bottom of the prestressed anchor rods



(a) Axial force at the top of the prestressed anchor rods



(b) Axial force at the middle of the prestressed anchor rods



(c) Axial force at the bottom of the prestressed anchor rods

Thereafter, the increase of the axial forces for all the anchor rods was very small during the monitoring period from the eighteenth month to the thirty-sixth month. At the end of the monitoring period, the axial forces at points A1-1, B1-1, and C1-1 were 22.11kN, 32.474 kN and 31.32 kN, respectively.

The analysis results of the axial force at the bottom of the prestressed anchor rods (refer to Fig. 13) are illustrated in Fig. 14c. The prestressed anchor rods were all under tension and continued to increase during the monitoring period. The axial force changes at the bottom of the anchor rods (refer to points A1-2, B1-2, and C1-2) went through three stages, i.e., rapid increase, slow increase, and gradual stabilization. This is similar to the characteristics of the axial force changes monitored at the top and middle of the anchor rods, shown in Fig. 14a and Fig. 14c. At the end of the monitoring period, the tension at points

A1-2, B1-2, and C1-2 were 14.221kN, 18.289kN and 11.104kN, separately.

The monitoring results (refer to Fig. 14) show that the maximum tensile force borne by the anchor rod was 41.471kN (i.e. point B1). As the diameter of the anchor rod was 25 mm, the calculated maximum tensile stress was 84.527 MPa at point B1 in the anchor rod-B.

5.2 Contact Pressure Between Initial Support Concrete and Surrounding Rocks

As shown in Fig. 15a, three measuring points (i.e. Point A2, B2 and C2) were arranged to monitor the contact pressure between the initial support concrete and surrounding rocks. Prior to the construction of the initial support, the earth pressure cells were installed. Then, the contact pressure was measured by the earth pressure cell, as illustrated in Fig. 15b.

Fig. 15 Contact pressure field monitoring. **a** measuring points, **b** installation of the earth pressure cell,

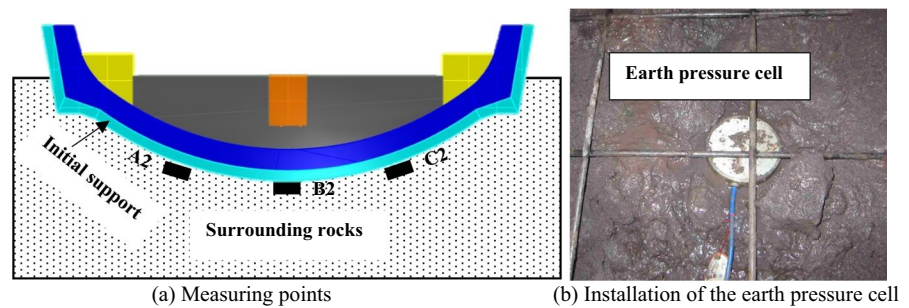
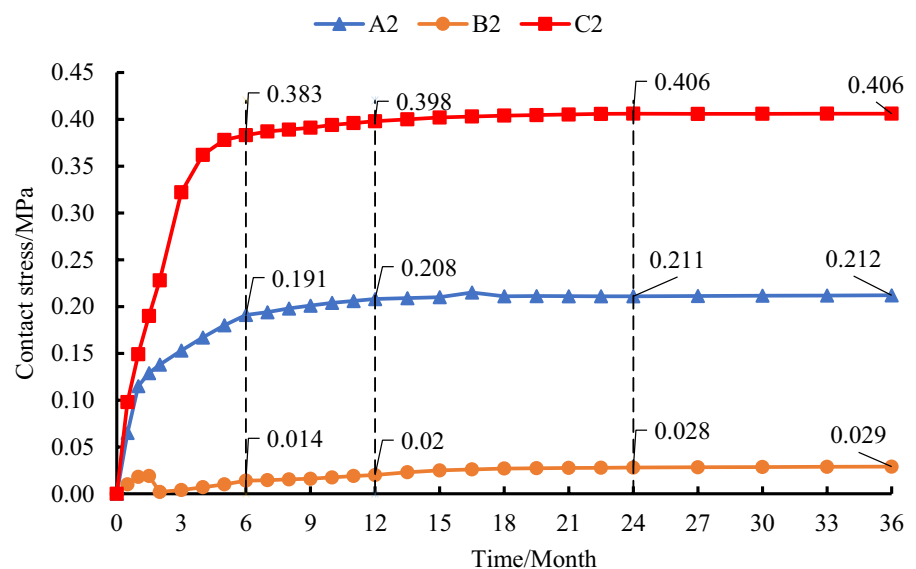


Fig. 16 Contact pressure between initial support concrete and surrounding rocks



The analysis results of contact pressure between initial support concrete and surrounding rocks are illustrated in Fig. 16. The contact pressure between the initial support concrete and surrounding rocks increased rapidly within the first six months. After the inverted arch structure was constructed, the contact pressure was adjusted to achieve balance. The contact pressure grew slower than before from the sixth to the twelfth month. The measured contact pressure in the twelfth month at points A2, B2, and C2 was 0.208 MPa, 0.02 MPa, and 0.398 MPa, respectively. After that, slow but steady growth in contact pressure was monitored from the twelfth month to the twenty-fourth month. The contact pressure ranged from rapid to slow transition from the beginning to the twenty-fourth month. This implies that the rheological effect of the tuff induced the continuous upward uplift of the surrounding rocks, increasing pressure on the initial support of the inverted arch. Later, from the twenty-fourth month to the thirty-sixth month, the contact pressure at point C2 remained stable, while the contact pressure change at points A2 and B2 was tiny. This indicates the contact pressure achieved a steady state at this stage. At the end of the monitoring period, the contact pressure between the initial support concrete and surrounding rocks at points A2, B2, and C2 was 0.212 MPa, 0.029 MPa, and 0.406 MPa, respectively.

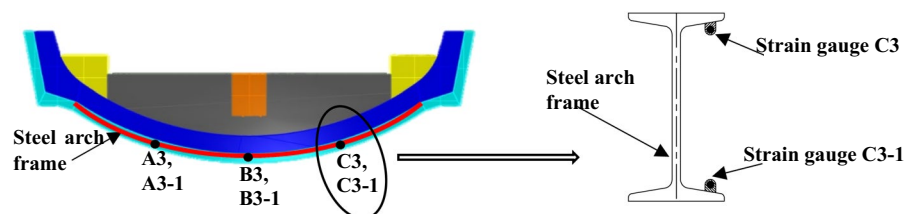
5.3 Stress of Initial Support

5.3.1 Layout of Measuring Points

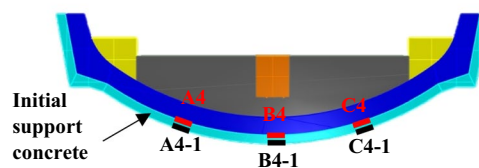
As shown in Fig. 17a, six measuring points (i.e. Point A3, A3-1, B3, B3-1, C3, and C3-1) were arranged to monitor the stress in the steel arch frame. Meanwhile, three measuring points (i.e. Point A3, B3, and C3) were arranged at the inner edge of the steel arch frame, while three measuring points (i.e. Point A3-1, B3-1, and C3-1) were arranged at the outer edge of the steel arch frame. The outer edge of the steel arch frame is close to the surrounding rocks, while the inner edge of the steel arch frame is adjacent to the secondary lining. Surface-mounted concrete strain gauges (JMZX-212) were used to monitor the stress of steel arch frames. Surface-mounted concrete strain gauges were welded to the inside of the upper and lower flanges of the steel arch frame.

As shown in Fig. 17b, six measuring points (i.e. Point A4, A4-1, B4, B4-1, C4, and C4-1) were arranged to monitor the stress in the initial support concrete. three Measuring points (i.e. Point A4, B4, and C4) were arranged at the inner edge of the initial support concrete, while three measuring points (i.e. Point A4-1, B4-1, and C4-1) were arranged at the outer edge of the initial support concrete. The outer edge of the initial support concrete is close to the surrounding rocks, while the inner edge of the initial support concrete is adjacent to the secondary lining.

Fig. 17 Measuring points arranged in initial support. **a** Measuring points on the steel arch frame. **b** Measuring points in initial support concrete

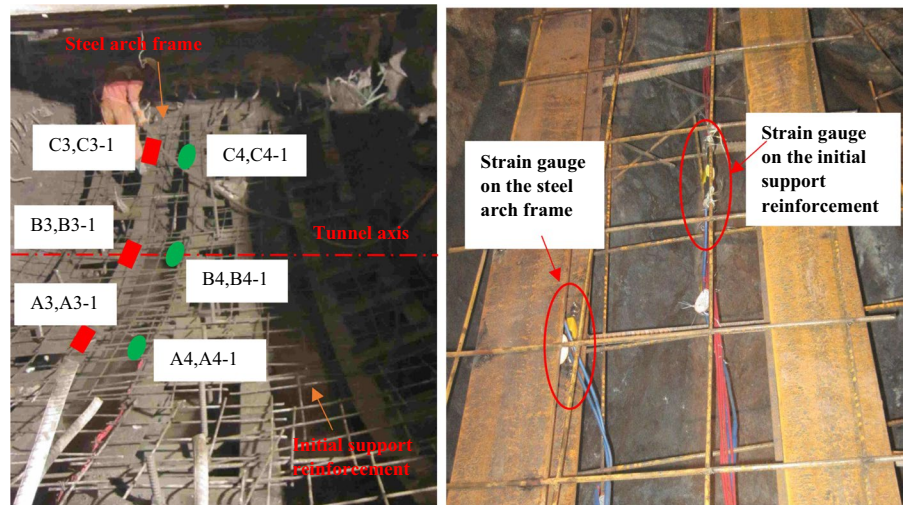


(a) Measuring points on the steel arch frame



(b) Measuring points in initial support concrete

Fig. 18 Field stress monitoring of initial support. **a** layout of measuring points. **b** Installation of strain gauges



(a) Layout of measuring points

(b) Installation of strain gauges

Embedded concrete strain gauges (JMZX-215) were used to monitor the stress of initial support concrete.

The field layout of these monitoring points in the steel arch frame and initial support concrete is illustrated in Fig. 18a. The installation of strain gauges on the steel arch frame and initial support concrete are illustrated in Fig. 18b.

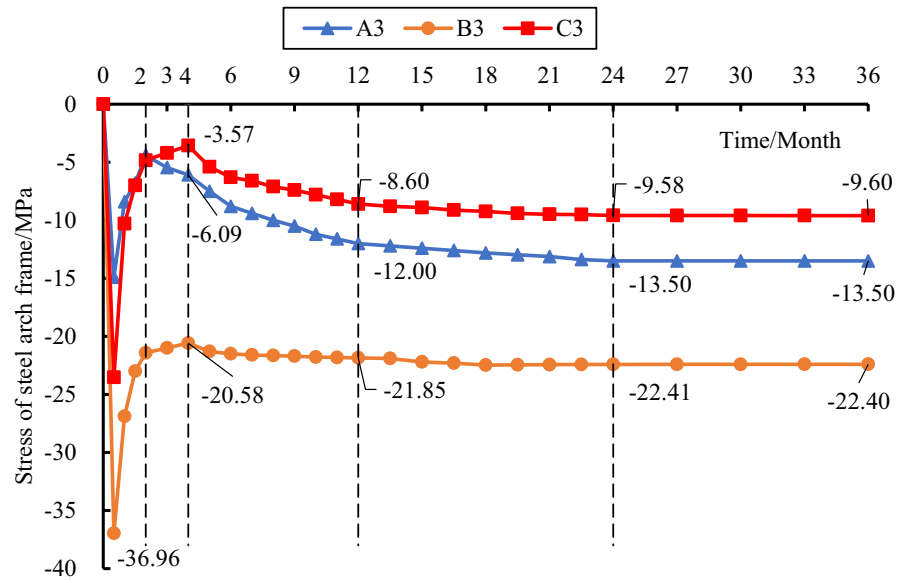
5.3.2 Stress of Steel Arch Frame

Figure 19a presents the monitoring results at the inner edge of the steel arch frame stress. The stress in steel arch frames was negative, indicating compressive stress. Steel arch frames began to bear loads immediately after completion, and the compressive stress in steel arch frames increased rapidly, with a maximum compressive stress of 36.96 MPa (i.e. at Point B3). Later, from the second to the fourth month, the stresses at points B3 and C3 gradually decreased, while the stress at point A3 steadily increased. Afterwards, the compressive stress of the steel arch increased until the twelfth month. The compressive stress in the twelfth month at points A3, B3, and C3, was 12 MPa, 21.85 MPa, and 8.6 MPa, respectively. Next, a slowing trend of increase appeared in the steel arch frame from the twelfth to the twenty-fourth month, implying that the stress of the steel arch frame was gradually adjusted and tended to be steady in the initial support. From the twenty-fourth to the thirty-sixth month, the stress of the steel arch changed very

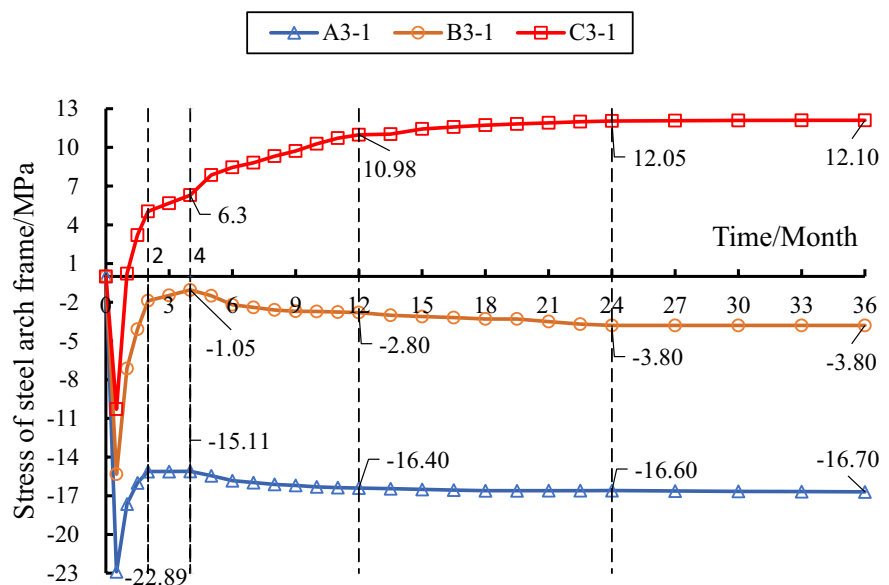
little and eventually reached a steady state. The compressive stress on the inner edge the steel arch frame at points A3 and C3 was 13.5 MPa and 9.6 MPa, respectively. Moreover, the ultimate maximum compressive stress of the steel arch frame was 22.4 MPa (i.e. at Point B3).

Figure 19b shows the monitoring results of stress at the outer edge of the steel arch frame. During the first two months of the monitoring period, the stresses at points A3-1, B3-1, and C3-1 in steel arch frames were negative, indicating compressive stress. The compressive stress in steel arch frames increased rapidly at the beginning of the monitoring period, with a maximum compressive stress of 22.89 MPa (i.e. at Point A3-1), implying that steel arch frames began to bear loads immediately after completion. Later, the stresses in the steel arch frame were adjusted and gradually reduced. At the end of the second month of the monitoring period, measurement points A3-1 and B3-1 were still subjected to compressive stresses, while the stress at point C3-1 was positive, indicating a tensile stress. Then, from the second to the fourth month, the change in stress at point A3-1 was very small, the stress at point B3-1 still gradually decreased, while the stress at point C3-1 steadily increased. The stress at the end of the second month at points A3-1, B3-1, and C3-1, was -15.11 MPa, -1.05 MPa, and 6.3 MPa, respectively. Afterwards, the stress of the steel arch increased until the twelfth month.

Fig. 19 Stress of steel arch frame. **a** Stress at the inner edge of steel arch frame. **b** Stress at the outer edge of steel arch frame



(a) Stress at the inner edge of steel arch frame

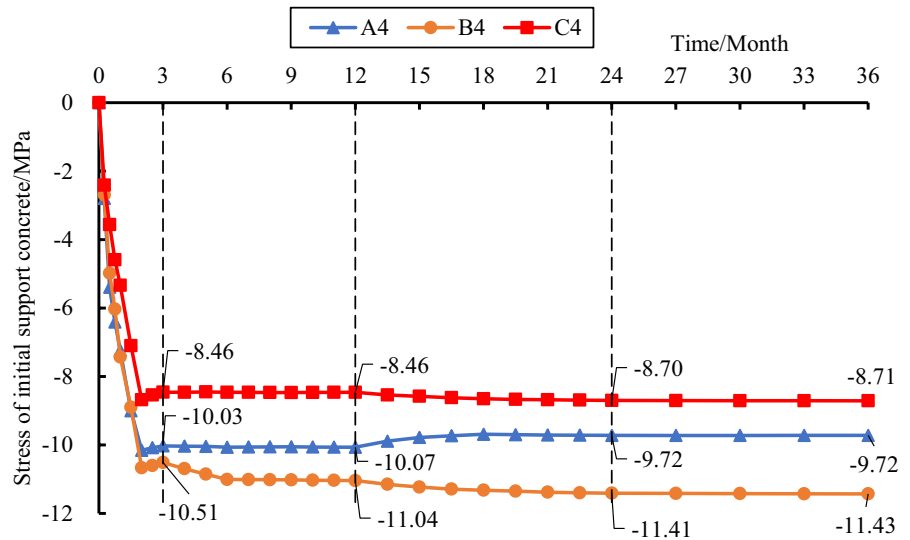


(b) Stress at the outer edge of steel arch frame

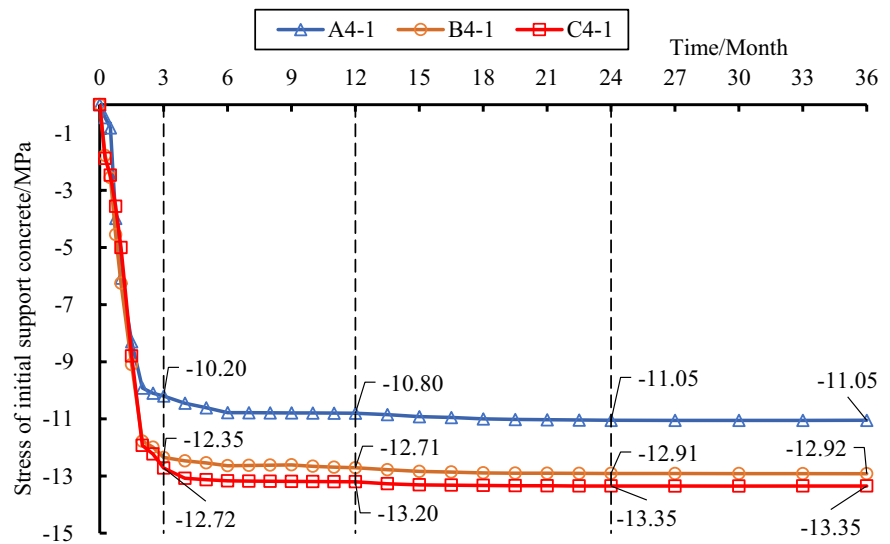
The compressive stress in the twelfth month at points A3-1 and B3-1 was 16.4 MPa and 2.8 MPa, respectively. Additionally, the tension stress at point C3-1 was 10.98MPa at the end of the twelfth month. Next, a slowing trend of increase appeared in the steel arch frame from the twelfth to the twenty-fourth month, implying that the stress of the

steel arch frame was gradually adjusted. From the twenty-fourth to the thirty-sixth month, the stress of the steel arch changed very little and finally reached a steady state. At the end of the monitoring period, the ultimate maximum compressive stress at the outer edge of the steel arch frame was 16.7 MPa at Point A3-1, and the maximum tensile stress at the

Fig. 20 Stress of initial support concrete. **a** Stress at the inner edge of initial support concrete. **b** Stress at the outer edge of initial support concrete



(a) Stress at the inner edge of initial support concrete



(b) Stress at the outer edge of initial support concrete

outer edge of the steel arch frame was 12.1 MPa at Point C3-1. Additionally, point B3-1 was subjected to compressive stress, 3.8 MPa.

5.3.3 Stress of Initial Support Concrete

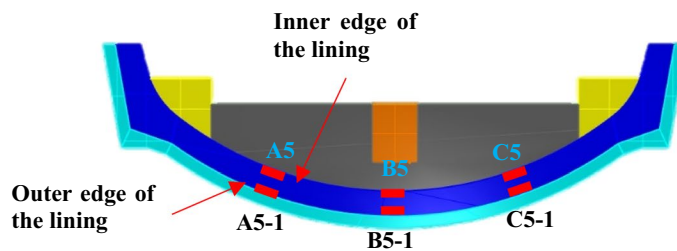
The monitoring results at the inner edge of initial support concrete stress are illustrated in Fig. 20a. During the whole monitoring period, the stress of the initial support concrete in the inverted arch was negative, indicating compressive stress. Within three

months after the completion of the inverted arch construction, the initial concrete support stress showed a rapid growth trend. It suggests that the initial support concrete resisted the deformation of the surrounding rock and bore considerable compressive stress. From the third to the twelfth month, the compressive stress of the initial support concrete at points A4 and B4 increased slower than before, while the stress at point C4 remained steady. It implies that the concrete stress gradually stabilized during this period. The concrete compressive stress in the twelfth month at

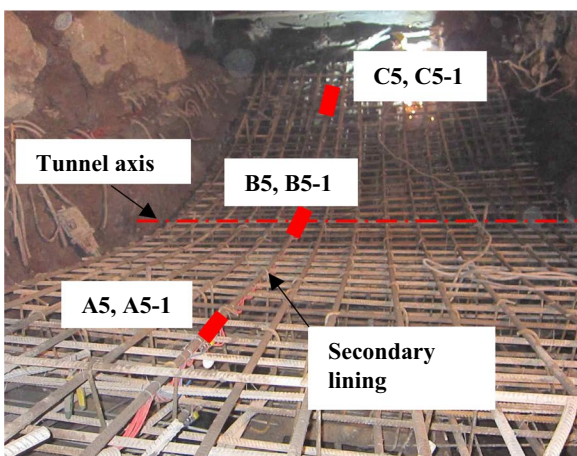
points A4, B4, and C4, was 10.07 MPa, 11.04 MPa, and 8.46 MPa, respectively. From the twelfth to the twenty-fourth month, A minor increase appeared in compressive stress of the initial support concrete at points B4 and C4, while a slight decrease appeared at point A4. Later, the initial support for concrete stress remained almost steady from the twenty-fourth to the thirty-sixth month. At the end of the monitoring period, the concrete compressive stress at points A4, B4, and C4 at the inner edge of initial support concrete was 9.72 MPa, 11.43 MPa, and 8.71 MPa, respectively. The monitoring results showed that the ultimate compressive stress of the initial support concrete was 11.43 MPa at point B4.

The stress monitoring results at the outer edge of the initial support concrete are illustrated in Fig. 20b. During the whole monitoring period, the stress of the initial support concrete at the outer edge of the inverted arch was negative, indicating compressive

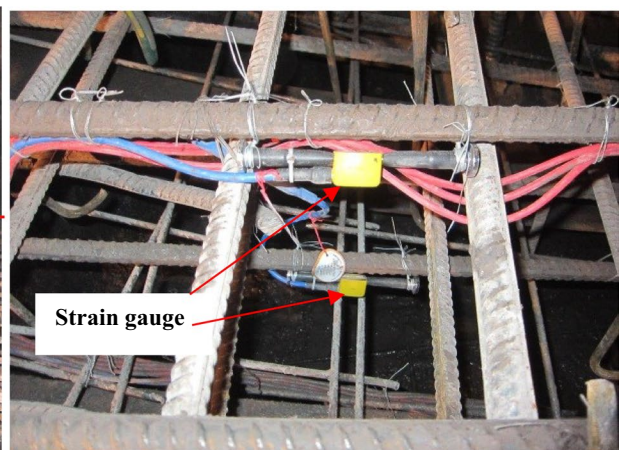
stress. The compressive stress in the initial support concrete increased rapidly at the beginning of the monitoring period. At the end of the third month of the monitoring period, the compressive stress at points A4-1, B4-1, and C4-1 in the initial support concrete reached 10.2 MPa, 12.35 MPa and 12.72 MPa, separately. From the third to the twelfth month, the compressive stress of the initial support concrete increased slower than before. The increase in stress at points A4-1, B4-1 and C4-1 was 0.6 MPa, 0.36 MPa and 0.48 MPa, respectively. It implies that the concrete stress gradually stabilized during this period. The concrete compressive stress in the twelfth month at points A4-1, B4-1, and C4-1, was 10.8 MPa, 12.71 MPa, and 13.2 MPa, respectively. From the twelfth to the twenty-fourth month, A minor increase appeared in compressive stress at the outer edge of the initial support concrete. Then, the stress at the outer edge of initial support concrete remained



(a) Measuring points in secondary lining concrete



(b) Layout of measuring points



(c) Installation of the strain gauge

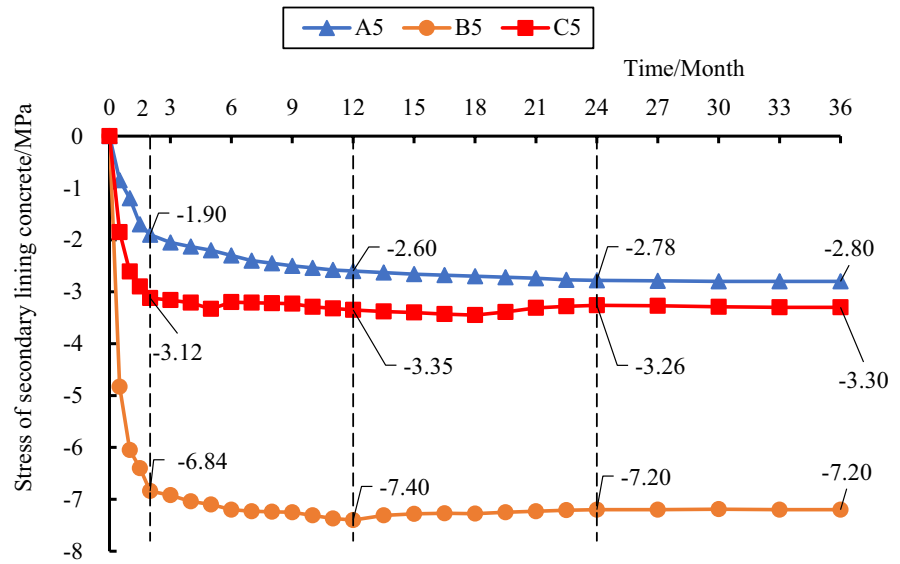
Fig. 21 Control measures of the inverted arch. **a** Measuring points in secondary lining concrete. **b** Layout of measuring points. **c** Installation of the strain gauge

almost steady from the twenty-fourth to the thirty-sixth month. At the end of the monitoring period, the concrete compressive stress at points A4-1, B4-1, and C4-1 at the outer edge of initial support concrete was 11.05 MPa, 12.92 MPa, and 13.35 MPa, respectively. The monitoring results showed that the ultimate compressive stress at the outer edge of the initial support concrete was 13.35 MPa at point C4-1.

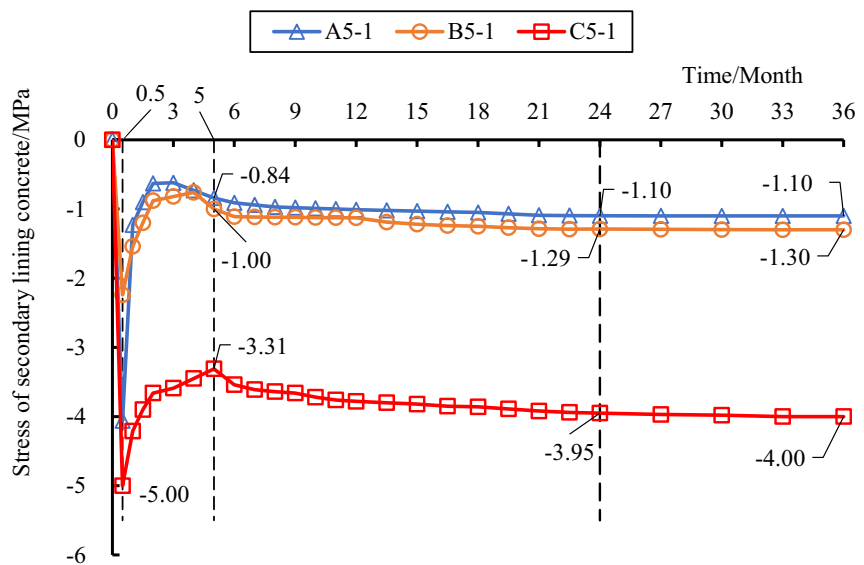
5.4 Stress of Secondary Lining Concrete

As shown in Fig. 21a, six measuring points (i.e. Point A5, A5-1, B5, B5-1, C5 and C5-1) were arranged to monitor the stress of secondary lining concrete in the inverted arch. Points A5, B5, and C5 were arranged at the inner edge of the secondary lining concrete in the inverted arch, while points A5-1, B5-1 and C5-1 were arranged at the

Fig. 22 Stress of secondary lining concrete. **a** Stress at the inner edge of secondary lining concrete. **b** Stress at the outer edge of secondary lining concrete



(a) Stress at the inner edge of secondary lining concrete



(b) Stress at the outer edge of secondary lining concrete

outer edge of the inverted arch lining concrete. The inner edge of the secondary lining is adjacent to the inverted arch filling layer, while the outer edge of the secondary lining concrete is close to the surrounding rocks. The field layout of these monitoring points is illustrated in Fig. 21b. Embedded concrete strain gauges (JMZX-215) were used to monitor the stress of secondary lining concrete. Embedded concrete strain gauges were tied with steel wire to the main reinforcement in the secondary lining structure, as shown in Fig. 21c.

Figure 22a depicts the monitoring results of concrete stress at the inner edge of the secondary lining. The secondary lining concrete stress in the inverted arch was negative, indicating compressive stress. In the first two months of the monitoring period, the compressive stress in the inverted arch concrete lining increased quickly, implying that the concrete lining began to bear loads after the inverted arch lining was completed. A continuous but slow growth appeared in the lining stress from the second to the twelfth month. This is probably due to the constant deformation of the surrounding rock caused by rheology, resulting in an increasing pressure acting on the lining. In the twelfth month, the concrete compressive stress at points A5, B5, and C5 was 2.60 MPa, 7.40 MPa, 3.35 MPa, respectively. The secondary lining bears loads together with the initial support, so the stress of the secondary lining concrete was gradually adjusted and tended to be steady from the twelfth to the twenty-fourth month. The stress at points B5 and C5 slightly reduced, while the stress at point A5 increased somewhat. Thereafter, the compressive stress of the steel arch remained almost steady from the twenty-fourth to the thirty-sixth month. At the end of the monitoring period, the compressive stress at the inner edge of secondary lining concrete in the inverted arch at points A5 and C5 was 2.80 MPa and 3.30 MPa, respectively. Moreover, the ultimate maximum compressive stress at the inner edge was 7.20 MPa (i.e. at Point B5).

Figure 22b depicts the monitoring results of concrete stress at the outer edge of the secondary lining in the inverted arch. The secondary lining concrete was subjected to compressive stress during the monitoring period. During the first half month of the monitoring period, the compressive stress at the outer edge of the secondary lining in the inverted arch increased quickly, implying that the concrete lining began to

bear loads after the inverted arch lining was completed. The maximum compressive stress at points A5-1, B5-1 and C5-1 reached 4.1 MPa, 2.2 MPa and 5.0 MPa, respectively. From the half month to the end of the fifth month, the compressive stresses at points A5-1 and B5-1 gradually decreased and rebounded, while the compressive stress at point C5-1 continued to decrease. This indicates that the stresses were gradually adjusting and the secondary lining structure and the initial support structure were sharing the load together. At the end of the fifth month, the concrete compressive stress at points A5-1, B5-1, and C5-1 was 0.84 MPa, 1.0 MPa, and 3.31 MPa, respectively. Then, the stresses at the outer edge of the secondary lining show similar variation characteristics as those at the inner edge. A continuous but slow growth appeared in the lining stress from the fifth to the twenty-fourth month. The increase in compressive stress at both points A5-1 and B5-1 was approximately 0.3 MPa, while the increase in compressive stress at point C5-1 was 0.64 MPa. In the twenty-fourth month, the concrete compressive stress at points A5-1, B5-1, and C5-1 was 1.1 MPa, 1.29 MPa, and 3.95 MPa, respectively. Thereafter, the compressive stress of the secondary lining concrete remained steady from the twenty-fourth to the thirty-sixth month. At the end of the monitoring period, the compressive stress at the outer edge of secondary lining concrete at points A5-1 and B5-1 was 1.10 MPa and 1.30 MPa, respectively. Moreover, the ultimate maximum compressive stress at the outer edge was 4.0 MPa at Point C5-1 from the monitoring results.

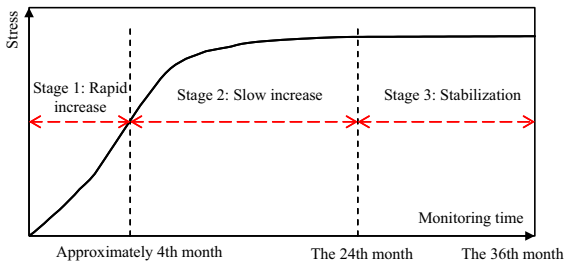
5.5 Stress Characteristics of the Inverted Arch Structure

5.5.1 Comparison of Field Observation Results of Sanlian Tunnel with Similar Projects

Table 8 shows the comparison of field monitored stresses of the Sanlian Tunnel with similar projects. As a result, it can be confirmed that the field monitoring results in this tunnel are reliable. As the inverted arch heaving occurred in the grade V tuff formation in this tunnel, field monitoring results of other tunnels excavated in grade V surrounding rocks were selected for comparison. As seen in Table 8, the stress distribution characteristics

Table 8 Comparison of Sanlian Tunnel with similar projects

Items for comparison	Field monitored stresses in this tunnel	Field monitored stresses in similar projects	Reference
Contact pressure between initial support concrete and surrounding rocks	Average contact pressure is 0.216 MPa	Grade V laminar stratum, average contact pressure is 0.377 MPa	Li et al. 2020
Stress of steel arch frame	All but one of the measuring points were subjected to compressive stresses ranging from 3.80 MPa to 22.40 MPa	Grade V stratum, most measuring points were subjected to compressive stresses of approximately 14.5 MPa to 46.8 MPa	Cao et al. 2018
Compressive stress of initial support concrete	The maximum compressive stress is 13.35 MPa	Grade V tuff stratum, the maximum compressive stress is 13.47 MPa	He et al. 2024
Stress of secondary lining concrete	The maximum compressive stress is 7.2 MPa	Grade V mudstone stratum, the maximum compressive stress is 8.5 MPa	Du et al. 2020

**Fig. 23** Development trend of the inverted arch stress

of the tunnel structure monitored in this work are roughly consistent with those of similar tunnels. The measured stresses of the tunnels are not exactly the same due to the different types of surrounding rocks and the variation in design and construction conditions. By comparison, it can be inferred that the field monitoring results of this work are reliable

and can be used to evaluate the structural safety of the repaired inverted arch.

5.5.2 Long-Term Stress Characteristics of the Inverted Arch

The inverted arch field monitoring results suggest that the anchor rod stress, initial support stress, and secondary lining stress underwent three stages: rapid increase, slow increase, and gradual stabilization, as shown in Fig. 23. Figure 23 only shows the development trend of stresses, the exact values of stresses can be seen in Figs. 14, 19, 20, and 22. The inverted arch structure was subjected to loads immediately after the construction, and thus the monitored stresses showed a rapid increase. Then, the rheology of the tuff rocks extruded the inverted arch structure, resulting in a continuous slow increase in the monitored stresses. Two years after the completion of the inverted arch, the rheological deformation of the surrounding

Table 9 Stress distribution of the inverted arch structure (Unit:MPa)

Structure	Location	Monitoring points on the left	Monitoring points in the middle	Monitoring points on the right	Location of the maximum stress	Average compressive stress
Stress of the steel arch frame	Inner edge	– 13.35	– 22.40	– 9.60	Middle	– 13.17
	Outer edge	– 16.70	– 3.80	12.10	Left	
Stress of initial support concrete	Inner edge	– 9.72	– 11.43	– 8.71	Middle	– 11.20
	Outer edge	– 11.05	– 12.92	– 13.35	Right	
Stress of secondary lining concrete	Inner edge	– 2.80	– 7.20	– 3.30	Middle	– 3.28
	Outer edge	– 1.10	– 1.30	– 4.00	Right	

rocks tended to stabilize, and thus the stresses in the inverted arch also show a gradual stabilization state.

Table 9 depicts the stress distribution of the inverted arch structure at the end of the monitoring period. The positive stress indicates tensile stress, while the negative stress indicates compressive stress. The inverted arch structure was mainly subjected to compressive stresses, and only one monitoring point at the outer edge of the steel arch frame was subjected to tensile stresses (i.e., 12.10 MPa). The maximum stresses mostly occurred in the middle of the inverted arch, implying that the middle of the inverted arch was subject to the maximum surrounding rock pressure. The average compressive stress of the steel arch frame (i.e., 13.17 MPa) was greater than that of the initial support concrete (i.e., 11.20 MPa). The steel arch frame was very stiff and could share more significant stresses. The secondary lining bore minimal compressive stresses (i.e., 3.28 MPa), indicating that the secondary lining had considerable safety reserves in the inverted arch structure.

5.6 Safety Evaluation of the Inverted Arch After Maintenance

5.6.1 Allowable Stress of Inverted Arch Structure

The maximum stresses at the end of the monitoring period are illustrated in Table 10. The strength limits of different materials in this table are obtained from Code for Design of Railway Tunnel (China Railway Eryuan Engineering Group Co.Ltd. 2016). Table 10 illustrates that the maximum stresses of the pre-stressed anchor bolt, the steel arch frame, the initial support concrete, and the secondary lining concrete were separately less than the allowable stress. Thus, after maintenance, the inverted arch is in a safe state.

5.6.2 Safety Factor of Inverted Arch Lining

Based on the secondary lining stresses at the end of the monitoring period in Fig. 22, the axial force N and bending moment M of the secondary lining are calculated according to Eqs. (4) and (5) (Wang et al. 2024). Positive axial forces represent tension, while negative axial forces represent pressure. Positive bending moments represent tension on the outside of the lining, while negative bending moments represent tension on the inside. The outside is close to the surrounding rocks, while the inside is adjacent to the tunnel clearance.

$$N = \frac{1}{2}bh(\sigma_1 + \sigma_2) \tag{4}$$

$$M = \frac{1}{12}bh^2(\sigma_1 - \sigma_2) \tag{5}$$

where b is the width of the calculated cross-section, i.e., 1 m along the longitudinal axis of the tunnel. h is the thickness of the secondary lining, i.e., 0.55 m. σ_1 is the stress acting at the outer edge of the lining, and σ_2 is the stress acting at the inner edge.

Figure 24 illustrates the calculated axial force and bending moment values at three sections (refer to A~C) in the secondary lining of the inverted arch after maintenance. As shown in Fig. 24a, negative axial forces, namely pressure, are applied in the lining structure. The axial force value at Section A, B and C in the secondary lining of the inverted arch is 1072.5kN, 2337.5kN and 2007.5kN, respectively. The maximum axial force value is 2337.5kN and is located at section B in the middle section of the inverted arch secondary lining. As shown in Fig. 24b, positive bending moments are applied in Section A and B in the secondary lining, indicating

Table 10 Summary of monitoring results

Materials	Maximum stress (MPa)	Allowable stress (MPa)
Prestressed anchor bolts (HRB400)	84.527 (tensile stress)	210
Steel arch frame (HPB300)	12.1 (tensile stress)	160
Steel arch frame (HPB300)	22.4 (compressive stress)	160
Initial support concrete (C25)	13.35 (compressive stress)	23.8
Secondary lining concrete(C35)	7.2 (compressive stress)	32.5

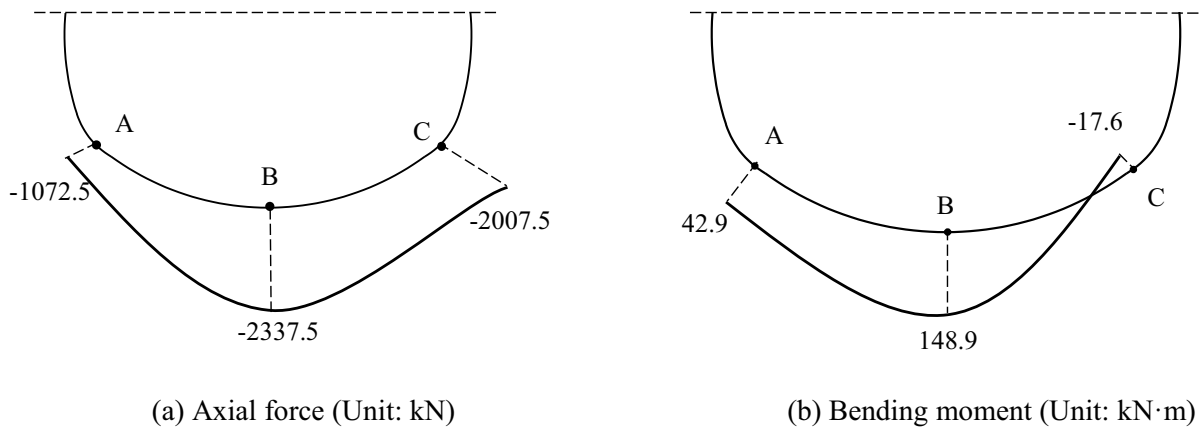


Fig. 24 Inner force of inverted arch lining after maintenance. **a** Axial force (Unit: kN). **b** Bending moment (Unit: kN·m)

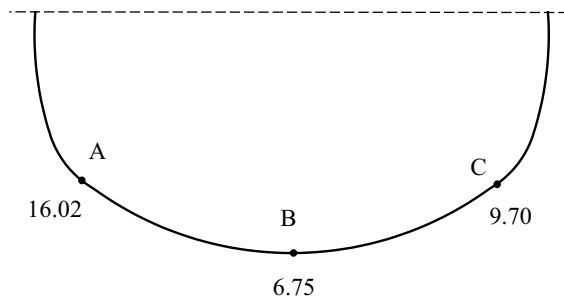


Fig. 25 Safety factor of inverted arch lining after maintenance

tension on the outside of the lining. Additionally, negative bending moment is applied in Section C in the secondary lining, indicating tension on the inside of the lining. The bending moment value at Section A, B and C in the secondary lining of the inverted arch is 42.9kN·m, 148.9kN·m and 17.6kN·m, respectively. The maximum bending moment value is 148.9kN and is located at section B in the middle section of the inverted arch secondary lining.

Secondly, based on the inner force values (shown in Fig. 24), the safety factors of the inverted arch secondary lining are calculated according to the Code for Design of Railway Tunnel (China Railway Eryuan Engineering Group Co.Ltd. 2016). The safety factors for critical sections (refer to A~C) are shown in Fig. 25. The safety factors in sections A, B, and C are 16.02, 6.75, and 9.7, respectively. The maximum safety factor is 16.02, located in section A. The

minimum safety factor is 6.75, located in section B, in the middle of the inverted arch. The safety factors at the two sides (refer to points A and C in Fig. 25) of the inverted arch are larger than that of the middle (refer to point B in Fig. 25). As can be seen Condition 2 in Table 6, safety factors at the two sides (refer to points A, B, D, E) are greater than that in the middle (refer to point C). The safety factors calculated by the numerical simulation and the field observation have similar characteristics, which indicates the reliability of the numerical analysis and field observation results. As illustrated in Code for Design of Railway Tunnel (China Railway Eryuan Engineering Group Co.Ltd.,2016), the safety factor of concrete lining must be greater than 2.4. These safety factors (refer to Fig. 25) meet the requirement. Therefore, the secondary lining structure of the rebuilt inverted arch is safe, and the maintenance of the inverted arch in the Sanlian Tunnel may achieve a good effect.

Although the two-dimensional numerical simulation used in this work was able to derive the cause of the inverted arch heaving, deformations of the inverted arch along the longitudinal axis of the tunnel could not be grasped. The tunnel construction encounters varying geological conditions, it is still not known whether the maintenance proposed in this work is applicable to other geological conditions other than tuff. Therefore, examining the longitudinal deformation characteristics by three-dimensional analysis and proposing maintenance suitable for a wide range of geological conditions will be the next research focuses.

6 Conclusion

By providing an overview of the inverted arch heaving in tuff formation in the SL Tunnel, this study has explored the cause and maintenance of the heaving. The numerical analysis using FLAC3D was conducted to investigate the cause of the inverted arch heaving. Then, field monitoring of stresses lasting for three years in the rebuilt inverted arch was undertaken to evaluate the effectiveness of maintenance. The following conclusions can be derived:

1. The field investigation shows that the maximum heaving on the inverted arch was 85 mm. Cracks with a width of 5~15mm and flexural deformation of reinforcement were also observed. The numerical simulation results indicate that the rheological effect of tuff is the main reason for the uplift and cracking of the inverted arch. It is possible to conclude that the structural design of the SL tunnel omitted the effect of tuff rheology and that the structural design needs to be optimized.
2. The proposed maintenance consists of removing the damaged inverted arch and constructing a new one. The depth of the rebuilt inverted arch was determined by a comparative analysis of numerical simulations for three working conditions. Deepened inverted arch structure by 65cm combined with 8m-long prestressed anchor rods were adopted to control the inverted arch distress.
3. After maintenance, the stresses of the inverted arch were observed for three years to evaluate the maintenance effect. Influenced by the long-term rheology of the tuff, the stresses in the inverted arch underwent three stages: rapid increase, slow increase, and gradual stabilization. The maximum stress of prestressed anchor rods, steel arch frames, initial support concrete, and secondary lining concrete were 84.53MPa, 22.40MPa, 13.35MPa, 7.20MP, respectively, which were lower than the permissible stress (namely 210MPa, 160MPa, 23.8MPa, 32.5MPa, respectively). Furthermore, the minimum safety factor (namely 6.75) calculated by the field monitoring results met the requirements (greater than 2.4) specified by the Code for Design of Railway Tunnel, signifying the safety of the inverted arch.
4. This study has improvement in the following three aspects. (i) Numerical simulations using

experimentally obtained material parameters reveal that tuff rheology is responsible for the inverted arch heaving. (ii) Deepened inverted arch structure combined with prestressed anchor rods are proposed to manage the inverted arch heaving of tunnels excavated in tuff deformation. (iii) The field stress observation lasting for three years is implemented to analyze the development of stresses in the inverted arch structure after maintenance. The proposed maintenance measures for addressing inverted arch distress are anticipated to yield positive results.

5. Tuff formation is widely distributed in southwest China. With the development of transportation infrastructure, more and more tunnels will be excavated in tuff strata. The suggested control technology holds substantial promise for practical implementation in engineering scenarios in tuff stratum. The designers and constructors of tunnels can learn from the design strategy of the inverted arch proposed in this work to ensure the safety of the tunnel structure.

Acknowledgements The authors would like to acknowledge the support of this research by Sanlian Tunnel Project Department of Chinese Railway Tunnel Group Limited.

Author contributions YW: Conceptualization, methodology, software, validation, investigation, data curation, formal analysis, funding acquisition, writing-original draft preparation, project administration and revision. HM: writing-review and editing, conceptualization (goals and aims). TKD: writing-review and editing. JG: funding acquisition.

Funding This work was funded by the National Natural Science Foundation of China under Grant No. 52302020.

Data availability Enquiries about data availability should be directed to the authors. The collected data is available upon request.

Declarations YW and JG report financial support was provided by National Natural Science Foundation of China under Grant No. 52302020. If there are other authors, they declare that they have no known competing financial interests or personal relationships that could have appeared to influence the work reported in this paper.

Conflict of interest The authors have no relevant financial or non-financial interests to disclose.

References

- Abdellah W, Butt S, Abdullah A, Towfeek A, Ali M (2024) Investigating the influence of geometric factors on tunnel stability: a study on arched roofs. *Geotech Geol Eng* 42:207–234. <https://doi.org/10.1007/s10706-023-02565-8>
- Agarwal J, Sarkar R (2024) Greenfield settlements due to tunnelling using tunnel boring machine (TBM) in layered soils: a parametric study. *Sādhanā* 49:75. <https://doi.org/10.1007/s12046-023-02425-4>
- Cao C, Shi C, Lei M, Yang W, Liu J (2018) Squeezing failure of tunnels: a case study. *Tunn Undergr Space Technol* 77:188–203. <https://doi.org/10.1016/j.tust.2018.04.007>
- Chang Z, Mei H, Yan C, Shi Y, Zhu X, Lu Z, Jia Z (2024a) Health status evaluation of highway tunnel inverted arch based on variable weight and extension cloud model. *Eng Fail Anal* 157:107939. <https://doi.org/10.1016/j.engfailanal.2023.107939>
- Chang Z, Yan C, Xie W, Lu Z, Lan H, Mei H (2024b) Large-scale field tunnel model experience and time-dependent floor heave induced by humidification. *Tunn Undergr Space Technol* 145:105615. <https://doi.org/10.1016/j.tust.2024.105615>
- Chen Z, Li Z, He C, Ma C, Li X, Chen K, Zhang H, Liu M (2023) Investigation on seepage field distribution and structural safety performance of small interval tunnel in water-rich region. *Tunn Undergr Space Technol* 138:105172. <https://doi.org/10.1016/j.tust.2023.105172>
- China Railway Eryuan Engineering Group Co.Ltd (2016) Code for design of railway tunnel (TB 10003–2016). China Railway Publishing House Co. Ltd, Beijing
- China Renewable Energy Engineering Institute (2020) Code for rock tests in water and hydropower projects (SL/T 264–2020). China Water & Power Press, Beijing
- Chu Z, Liu B, Sun J, Shen J, Song Y, Li T (2018) Research on rheological similar material of soft rock based on Burgers model. *Chin J Rock Mech Eng* 37(05):1185–1198. <https://doi.org/10.13722/j.cnki.jrme.2017.1082>
- Ding Z, Huang X, Sun M, Xu L, Huang Z, Zhou Q (2023) Experimental study on the influence of cracks on tunnel vibration under subway train load. *Tunn Undergr Space Technol* 142:105444. <https://doi.org/10.1016/j.tust.2023.105444>
- Du M, Wang X, Zhang Y, Li L, Zhang P (2020) In-situ monitoring and analysis of tunnel floor heave process. *Eng Fail Anal* 109:104–111. <https://doi.org/10.1016/j.engfailanal.2019.104323>
- Elbady A, Mousa S, Mohamed H, Benmokrane B (2024) Contribution of closed ties to shear strength of GFRP-reinforced precast concrete tunnel lining segments: experimental and analytical study. *J Compos Constr* 28(3):04024006. <https://doi.org/10.1061/JCCOF2.CCENG-4361>
- Fei R, Peng L, Zhang C, Zhang J, Zhang P (2023) Experimental and numerical studies of a shield twin tunnel undercrossing the existing high-speed railway Tunnel. *Geotech Geol Eng*. <https://doi.org/10.1007/s10706-023-02650-y>
- Festi P, Bossi G, Francioni M, Marcato G, Staboli C, Borgatti L (2023) Structural health of a road tunnel intersecting a large and active rock-block slide. *Italan J Eng Geol Environ Spec Issue* 1:49–55. <https://doi.org/10.4408/IJGE.2023-01.S-07>
- Ghadernejad S, Moosavi M (2022) Predicting the displacement of a circular tunnel in an elastic medium exhibiting time-dependent swelling behavior. *Geotech Geol Eng* 40:2677–2690. <https://doi.org/10.1007/s10706-022-02053-5>
- Gilbert R, Bernard E (2018) Post-cracking ductility of fibre reinforced concrete linings in combined bending and compression. *Tunn Undergr Space Technol* 76:1–9. <https://doi.org/10.1016/j.tust.2018.02.010>
- Gong J, Tang G, Wang W, Fan L (2022) Statistics on railway tunnels in China and the design and construction of the Gaoligongshan Tunnel by the end of 2021. *Tunnel Constr* 42(3):508–517
- Han Z, Ma W, Chai J, Zhu Z, Lin C, An Z, Ma C, Xu X, Xu T (2021) A treatment technology for optimizing the stress state of railway tunnel bottom structure. *Shock Vib* 2021:1–13. <https://doi.org/10.1155/2021/9191232>
- Haque M, Ansary M (2023) Liquefiable concrete tunnel-sand-pile interaction response under seismic excitations. *Geotech Geol Eng* 42:409–431. <https://doi.org/10.1007/s10706-023-02580-9>
- He J, He S, Liu X, Ma J, Li Y, Zhang B (2024) Investigating the mechanical responses and construction optimization for shallow super-large span tunnels in weathered tuff stratum based on field monitoring and Flac3D modeling. *Int J Civ Eng* 22:379–395. <https://doi.org/10.1007/s40999-023-00891-9>
- Jia J, Chen Y, Luo H, Ma G (2023) Seepage stability analysis of a deep-buried tunnel in fractured rocks based on a non-Darcy hydro-mechanical coupled method. *Tunn Undergr Space Technol* 142:105393. <https://doi.org/10.1016/j.tust.2023.105393>
- Kong C, Gao X, Wang F, Wang H, Li H, Zhao X, Liu J, Zhang Y, Luo Y (2024) Analysis of mechanical properties and joint selection for secondary linings in drill and blast tunnels with prefabricated invert arch: case study of a single-line railway tunnel. *Tunn Undergr Space Technol* 144:105560. <https://doi.org/10.1016/j.tust.2023.105560>
- Kuang G, Li B, Mo S, Hu X, Li L (2022) Review on machine learning-based defect detection of shield tunnel lining. *Periodica Polytech Civ Eng* 66(3):943–957. <https://doi.org/10.3311/PPci.19859>
- Li S, Tan Z, Yang Y (2020) Mechanical analyses and controlling measures for large deformations of inclined and laminar stratum during tunnelling. *Geotech Geol Eng* 38:3095–3112. <https://doi.org/10.1007/s10706-020-01210-y>
- Li G, Zhai J, Luo C, Li A (2021) Research and application of automatic monitoring system for tunnel-surrounding rock measurement based on GIS. *Arab J Geosci* 14:1017. <https://doi.org/10.1007/s12517-021-07197-x>
- Li Z, Li Z, Huang W, Xu Z, Zhang W, Chen K (2022) Tunnel bottom cavity laws of heavy-haul railway tunnel under train load and groundwater in weak surrounding rock condition. *KSCE J Civ Eng* 26(3):1451–1464. <https://doi.org/10.1007/s12205-021-5953-y>
- Lin C, Wang X, Nie L, Sun H, Xu Z, Du Y, Liu L (2020) Comprehensive geophysical investigation and analysis of lining leakage for water-rich rock tunnels: a case study of Kaiyuan Tunnel, Jinan, China.

- Geotech Geol Eng 38:3449–3468. <https://doi.org/10.1007/s10706-020-01225-5>
- Liu S, Shi Y, Sun R, Yang J (2020) Damage behavior and maintenance design of tunnel lining based on numerical evaluation. *Eng Fail Anal* 109:104–113. <https://doi.org/10.1016/j.engfailanal.2019.104209>
- Ma K, Li W, Li J, Wang H, Zheng J, Zhang J (2020) Research on the mechanism and treatment technique of invert floor heave after the penetration of large cross-section tunnel in slight inclined stratum. *IOP Conf Ser Earth Environ Sci* 570:052031. <https://doi.org/10.1088/1755-1315/570/5/052031>
- Malkowski P, Ostrowski L, Stasica J (2022) Modeling of floor heave in underground roadways in dry and waterlogged conditions. *Energies* 15:4340. <https://doi.org/10.3390/en15124340>
- Min B, Zhang C, Zhu W, Zhang X, Li P (2021) Influence of cracks at the invert on the mechanical behavior of the tunnel structures. *Thin-Walled Struct* 161:107–119. <https://doi.org/10.1016/j.tws.2020.107405>
- Nicotera M, Russo G (2021) Monitoring a deep excavation in pyroclastic soil and soft rock. *Tunn Undergr Space Technol* 117:104130. <https://doi.org/10.1016/j.tust.2021.104130>
- Ouyang A, Murro V, Cull M, Cunningham R, Osborne J, Li Z (2023) Automated pixel-level crack monitoring system for large-scale underground infrastructure—a case study at CERN. *Tunn Undergr Space Technol* 140:105310. <https://doi.org/10.1016/j.tust.2023.105310>
- Petraroia D, Plückerlmann S, Mark P, Breitenbücher R (2024) Tunnel lining segments with enhanced bearing capacity using hybrid concrete concepts. *Tunn Undergr Space Technol* 143:105484. <https://doi.org/10.1016/j.tust.2023.105484>
- Qiu J, Zhou X, Shen Y, Zhang X, Yu B, Luo Y (2023) Failure mechanism of the deep-buried metro tunnel in mixed strata: Physical model test and numerical investigation. *Tunn Undergr Space Technol* 139:105224. <https://doi.org/10.1016/j.tust.2023.105224>
- Rao P, Meng J, Cui J, Nimbalkar S (2023) Field study on rectangular inclined deep foundation excavation in soft soils. *Geotech Geol Eng*. <https://doi.org/10.1007/s10706-023-02666-4>
- Reddy P, Mohanty B, Rao B (2020) Influence of clay content and montmorillonite content on swelling behavior of expansive soils. *Int J Geosynth Ground Eng* 6:1. <https://doi.org/10.1007/s40891-020-0186-6>
- Senthil K, Pelecanos L, Rupali S, Sharma R, Manish K (2024) Experimental and numerical investigation on soft soil tunnels under impact loading condition. *J Vib Eng Technol* 12:2175–2203. <https://doi.org/10.1007/s42417-023-00973-x>
- Song W, Lai H, Liu Y, Yang W, Zhu Z (2019) Field and laboratory study of cracking and safety of secondary lining for an existing highway tunnel in loess ground. *Tunn Undergr Space Technol* 88:35–46. <https://doi.org/10.1016/j.tust.2019.02.018>
- Trabucchi I, Smarslik M, Tiberti G, Petraroia D, Plizzari G, Mark P (2021) A hybrid solution proposal for precast tunnel segments. *Struct Concr* 22:1534–1548. <https://doi.org/10.1002/suco.202000629>
- Wang Y, Mansor H, David T (2024) Timely constructed and enhanced lining for managing extensive deformations of tunnel in coal stratum: a case study. *Open Civ Eng J* 18:e18741495284171. <https://doi.org/10.2174/0118741495284171231226062346>
- Xu Z, Yang J, Tao W, Wang L (2021) Study on relevant cases and occurrence mechanism of bottom heave in tunnel under high geo-stress. *Modern Tunn Technol* 58(1):265–276. <https://doi.org/10.13807/j.cnki.mtt.2021.S1.034>
- Yang J, Zhou K, Cheng Y, Gao Y, Wei Q, Hu Y (2019) Mechanism and control of roadway floor heave in the paleogene soft rock surroundings. *Geotech Geol Eng* 37:5167–5185. <https://doi.org/10.1007/s10706-019-00970-6>
- Ye F, Han X, Qin N, Ouyang A, Liang X, Xu C (2020) Damage management and safety evaluation for operating highway tunnels: a case study of Liupanshan tunnel. *Struct Infrastruct Eng* 2020:1–12. <https://doi.org/10.1080/15732479.2020.1713165>
- Yousif Q, Karakouzian M (2023) Distinct element modeling of uniaxial compression tests of tuff-like lithophysal material; using voronoi tessellation system. *Geotech Geol Eng* 41:319–335. <https://doi.org/10.1007/s10706-022-02284-6>
- Yue Y, Liu C, Hou Z, Qin Y (2023) Influencing factors and adaptability of working face length in deep thick coal seam. *Geotech Geol Eng* 41:2871–2886. <https://doi.org/10.1007/s10706-023-02432-6>
- Zertsalov M, Chunyuk D, Minin K, Polysaeva A (2022) Fiber-reinforced concrete lining of unpressurized hydraulic tunnels in rocks and determination of their crack resistance. *Power Technol Eng* 55:877–880. <https://doi.org/10.1007/s10749-022-01446-z>
- Zhang J, Li S, Li Z, Zhang Q, Yang L, Du J, Li H, Qi Y, Lin R (2020) Grouting effect on reinforcement of weathered granite. *Geotech Geol Eng* 38:2873–2886. <https://doi.org/10.1007/s10706-020-01193-w>
- Zhang J, Xiang X, Du R, Zhang X (2024) Enhancing tunnel stability under high ground stress: rheological analysis and support strategies. *Geotech Geol Eng*. <https://doi.org/10.1007/s10706-023-02730-z>

Publisher's Note Springer Nature remains neutral with regard to jurisdictional claims in published maps and institutional affiliations.

Springer Nature or its licensor (e.g. a society or other partner) holds exclusive rights to this article under a publishing agreement with the author(s) or other rightsholder(s); author self-archiving of the accepted manuscript version of this article is solely governed by the terms of such publishing agreement and applicable law.